

Banner appropriate to article type will appear here in typeset article

1 **A sparse optimal closure for a reduced-order model** 2 **of wall-bounded turbulence**

3 **Zhao Chua Khoo, Chi Hin Chan[†], and Yongyun Hwang**

4 Department of Aeronautics, Imperial College London, South Kensington, London SW7 2AZ, UK

5 (Received xx; revised xx; accepted xx)

6 In the present study, a set of physics-informed and data-driven approaches are examined
7 towards the development of an accurate reduced-order model for a turbulent plane Couette
8 flow. Based on the utilisation of the proper orthogonal decomposition (POD), a particular
9 focus is given to the development of a reduced-order model where the number of POD
10 modes are not large enough to cover the full dynamics of the given turbulent state, the
11 situation directly relevant to the reduced-order modelling for turbulent flows. Starting from
12 the conventional Galerkin projection approach ignoring the truncation error, three approaches
13 enhanced by both physics and data are examined: 1) sparse regression of the POD-Galerkin
14 dynamics; 2) Galerkin projection with an empirical eddy viscosity model; 3) Galerkin
15 projection with an optimal eddy viscosity obtained from a newly-proposed sparse regression
16 - an idea applying the Sparse Identification of Nonlinear Dynamics (SINDy) framework to an
17 eddy-viscosity model. The sparse regression of the POD-Galerkin dynamics does not perform
18 well, as the number of POD modes for the given chaotic dynamics appears to be too small.
19 While the unsatisfactory performance of the Galerkin projection model with an empirical
20 eddy viscosity is observed, the newly proposed approach, which combines the concept of an
21 optimal eddy-viscosity closure with a sparse regression, more accurately approximates the
22 chaotic dynamics than the other reduced-order models considered. This is demonstrated with
23 the mean and time scales of the POD mode amplitudes as well as the first- and second-order
24 turbulence statistics.

25 **Key words:** Low-dimensional models, Turbulent boundary layers

26 **1. Introduction**

27 1.1. *Dynamical systems approach for wall-bounded turbulence*

28 Coherent structures in turbulent flows have been studied for many decades. These highly
29 organised fluid motions in a chaotic flow field often carry significant amount of turbulent
30 kinetic energy and momentum. Understanding and modelling of their dynamics have been a
31 central challenge in turbulence research. In wall-bounded shear flows, a coherent structure
32 was first discovered in the near-wall region (Kline *et al.* 1967) and many different kinds of
33 coherent structures were subsequently observed over the past half century (e.g. Kovaszny

[†] Email address for correspondence: chi.chan19@imperial.ac.uk

34 *et al.* 1970; Falco 1977; Head & Bandyopadhyay 1981; Jeong *et al.* 1997; Kim & Adrian 1999;
35 del Álamo & Jiménez 2003; Hutchins & Marusic 2007, and many others). The growing
36 evidence suggests that these coherent structures are organised in the form of the so-called
37 ‘attached eddies’ originally hypothesised by Townsend (1956, 1976) for the logarithmic layer:
38 coherent structures in the logarithmic layer emerge in the form of a self-similar hierarchy and
39 their characteristic length scale is proportional to the distance between the eddy centre and
40 the wall (see Hwang & Lee 2020 for a mathematical proof). The attached eddy hypothesis
41 can be extended to include the near-wall and outer regions in a broad sense (Hwang 2015),
42 and there has been a growing body of evidence supporting this idea over the past decade
43 (see the recent review of Marusic & Monty 2019, and the references therein). In particular,
44 each of these attached eddies was found to retain a sustaining mechanism independent of the
45 others (Flores & Jiménez 2010; Hwang & Cossu 2010*c*, 2011; Hwang & Bengana 2016).
46 This mechanism has been referred to as the ‘self-sustaining process’ and is based on a quasi-
47 cyclic interaction of streaks and quasi-streamwise vortices (Hamilton *et al.* 1995; Waleffe
48 1997): 1) amplification of streamwise-elongated streaks by streamwise vortices through the
49 lift-up effect (Butler & Farrell 1993; del Álamo & Jiménez 2006; Cossu *et al.* 2009; Hwang
50 & Cossu 2010*a,b*); 2) breakdown of the amplified streaks via an instability and/or transient
51 growth (Hamilton *et al.* 1995; Schoppa & Hussain 2002; Park *et al.* 2011; Alizard 2015;
52 Cassinelli *et al.* 2017; de Giovanetti *et al.* 2017; Lozano-Durán *et al.* 2021); 3) nonlinear
53 regeneration of streamwise vortices (Hamilton *et al.* 1995; Schoppa & Hussain 2002; Hwang
54 & Bengana 2016). A key on-going challenge is to understand the interactions between the
55 self-sustaining processes at multiple length scales, and recent studies have suggested that the
56 interaction dynamics appear to be dauntingly complex (Cho *et al.* 2018; Lee & Moser 2019;
57 Doohan *et al.* 2021*b*).

58 The discovery of the self-sustaining process has played a central role in advancing the
59 notions of dynamical systems for turbulence research. In particular, it physically underpins
60 the existence of non-trivial unstable equilibrium and time-periodic solutions in wall-bounded
61 shear flows (Nagata 1990; Waleffe 2001; Kawahara & Kida 2001; Jiménez & Simens
62 2001; Waleffe 2003; Faisst & Eckhardt 2003; Wedin & Kerswell 2004; Gibson *et al.* 2008,
63 2009; Hall & Sherwin 2010; Park & Graham 2015; Hwang *et al.* 2016; Yang *et al.* 2019;
64 Doohan *et al.* 2019, and many others). These solutions form a state-space skeleton for the
65 birth of turbulence through a sequence of local and global bifurcations (Eckhardt *et al.*
66 2007; Kawahara *et al.* 2012; Graham & Floryan 2020), and their use has been central
67 to the description for the temporal dynamics of transition to turbulence (e.g. Kreilos &
68 Eckhardt 2012) and for the local behaviour in the spatio-temporal dynamics (see the review
69 by Barkley 2016). Furthermore, given that they are exact solutions to the Navier-Stokes
70 equations, they provide precise understanding for turbulence dynamics in an interpretable
71 and mathematically analysable manner especially compared to the structures obtained with
72 conventional conditional average.

73 Despite these advances, the computation of the unstable equilibrium and periodic solutions
74 are increasingly infeasible as Reynolds number increases. A key reason to this is that the
75 typical algorithms used for the search of these solutions are designed to iteratively find the
76 initial condition that leads to the same flow field after a given time interval (an arbitrary
77 small time interval for equilibrium and a time period for periodic orbits; e.g. Viswanath
78 2007; Willis *et al.* 2013; Farzmand 2016). Apart from the computational cost required for
79 the repeated simulations, the numerical convergence of such an algorithm depends on the
80 leading Lyapunov exponent of the related chaotic state – it becomes increasingly difficult
81 to find an initial flow field which converges with a sufficiently small residual when the
82 leading Lyapunov exponent is very large. An approach employed to bypass this difficulty
83 was to approximate the complex multi-scale dynamics at high Reynolds numbers with a

84 closure model (e.g. Rawat *et al.* 2015; Hwang *et al.* 2016; Yang *et al.* 2019). Yet, the
 85 unstable equilibrium and periodic solutions obtained with this strategy are often obtained
 86 by continuing the existing solutions at low Reynolds numbers, thereby not retaining the key
 87 multi-scale processes of interest at high Reynolds numbers (e.g. scale interactions). Indeed, a
 88 very recent work by Doohan *et al.* (2021a) showed that when turbulence exhibits multi-scale
 89 behaviours explicitly, most of the equilibrium solutions obtained in this manner do not sit
 90 anywhere near turbulent state in the physically relevant phase portraits. An obvious way to
 91 resolve this issue is to compute unstable periodic orbits with sufficiently long time periods, as
 92 they should be able to capture the key periodic and/or quasi-periodic multi-scale dynamics.
 93 However, in practice, their computation is much more difficult than that of the equilibrium
 94 solutions and is practically almost impossible due to the rapidly vanishing convergence of the
 95 solutions by the increasing Reynolds number. This poses an important challenge in extending
 96 the notions of dynamical systems for the description of multi-scale behaviours of turbulent
 97 flows.

98 Given this challenge, it is worth mentioning that many of the unstable equilibrium and
 99 periodic solutions have previously been computed in a highly reduced system even at low
 100 Reynolds numbers. Indeed, a large number of such solutions have been found in highly
 101 confined computational domains, in which the full spatio-temporal dynamics in a large
 102 computational domain would be drastically reduced (Nagata 1990; Waleffe 1995; Kawahara
 103 & Kida 2001; Jiménez & Simens 2001; Faisst & Eckhardt 2003; Wedin & Kerswell 2004;
 104 Gibson *et al.* 2008; Park & Graham 2015; Hwang *et al.* 2016; Doohan *et al.* 2019, 2021a). For
 105 the same rationale, perhaps, the key to tackling the multi-scale dynamics of turbulence using
 106 the dynamical systems notions may lie in a suitable dimensionality reduction of the given
 107 turbulent state without losing the core dynamics of interest. The equilibrium and periodic
 108 solutions to the reduced-order dynamical system can then be obtained much more easily
 109 using existing techniques, with hope that they can subsequently be used as proxies and/or a
 110 symbolic description for the multi-scale dynamics of a turbulent system.

111 1.2. *Reduced-order modelling*

112 Reduced-order modelling has been a long-standing topic in fluid mechanics, and wall-
 113 bounded turbulence is a flow configuration to which the earliest modelling efforts were made
 114 (Aubry *et al.* 1988; Rempfer & Fasel 1994a). The previous efforts may be classified into two
 115 categories. One is based on the proper orthogonal decomposition (e.g. Lumley 1967, 1981;
 116 Sirovich 1987; Holmes *et al.* 1996), and the reduced-order model is subsequently obtained
 117 by projecting the Navier-Stokes equations onto the space spanned by the POD modes (i.e.
 118 Galerkin projection; Aubry *et al.* 1988; Rempfer & Fasel 1994a,b; Smith *et al.* 2005). The
 119 other is equivalent to a heavily truncated spectral approximation to the system of interest
 120 (Waleffe 1997; Moehlis *et al.* 2004, 2005; Lagha & Manneville 2007; Chantry *et al.* 2017;
 121 Cavalieri 2021), which is often used to study low-dimensional dynamics of bifurcation and
 122 transition to turbulence. Given the scope of the present study, here we shall employ the
 123 former approach based on POD modes, as they provide the best orthonormal basis in terms
 124 of capturing the energy of the given flow fields.

125 One of the key challenges in the development of a reduced-order model using the POD
 126 modes are often associated with the number of POD modes considered and the resulting
 127 truncation. This problem becomes significant especially for high Reynolds number flows,
 128 where the small-scale motions, not captured by the chosen POD modes, play a crucial role in
 129 the energy cascade and turbulent dissipation. Indeed, one of the most fundamental features
 130 of turbulence is the exact balance between the production at large scale and the dissipation
 131 at the small (Kolmogorov) scale. Therefore, not accounting for such small-scale motions
 132 leads to an excess of energy and/or an erroneous behaviour in the reduced-order model.

133 This issue has often been resolved by incorporating an additional eddy-viscosity model that
134 removes the excess in the energy of the reduced-order model (Aubry *et al.* 1988; Rempfer
135 & Fasel 1994*b*; Couplet *et al.* 2005; Smith *et al.* 2005; Noack *et al.* 2011; Östh *et al.* 2014;
136 Protas *et al.* 2015). Given the scope of the present study, the approach of Protas *et al.* (2015)
137 is particularly appealing, in which an ‘optimal’ eddy viscosity was proposed to minimise
138 the difference between the data from the measurement and from the reduced-order model.
139 In this approach, the gradient of the given objective functional is computed over multiple
140 time intervals using the adjoint-based formulation. The best-performing eddy viscosity is
141 subsequently obtained by updating its value at every time interval, an approach reminiscent
142 of the ‘sub-optimal’ control in flow control problem (Choi *et al.* 1993; Lee *et al.* 1999). It is
143 worth mentioning that such an optimisation problem is ideally formulated with an objective
144 functional considering a long time interval. However, the resulting adjoint equation for the
145 Lagrange multiplier is mathematically unstable around the chaotic trajectory due to the
146 positive leading Lyapunov exponent. This inherently limits the size of the time interval that
147 can be used for the gradient calculation. Furthermore, the leading Lyapunov exponent rapidly
148 grows with the Reynolds number, forming an important challenge in the application of such
149 an approach for high Reynolds numbers – indeed, a similar issue of the time interval in the
150 adjoint-based optimisation problem was previously discussed in the context of an optimal
151 control problem (e.g. Bewley *et al.* 2001). Recently, there have been a rapidly growing
152 number of studies aiming to identify the governing dynamics solely from simulation and
153 experimental data available (e.g. Schmidt & Lipson 2009; Brunton *et al.* 2016; Loiseau &
154 Brunton 2018). In the context of fluid mechanics, a novel approach was proposed by Brunton
155 *et al.* (2016), who accurately identified the governing low-dimensional dynamics of Lorenz
156 chaos and the two-dimensional laminar cylinder wake from data. In their study, a reduced-
157 order model based on POD modes is identified in a data-driven manner by formulating an
158 l_1 -regularisation-based optimisation which minimises the difference between the full and
159 the reduced-order dynamics – the approach referred to as ‘sparse identification of nonlinear
160 dynamics (SINDy)’. Furthermore, the SINDy framework has been extended by Loiseau &
161 Brunton (2018), who introduced a constraint enforcing energy-preserving nonlinearity by
162 reformulating the sparse regression problem with the Karush-Kuhn-Tucker conditions. There
163 is also on-going effort to improve low-dimensional representation of nonlinear dynamics
164 by nonlinear correlations in the temporal POD coefficients (Callaham *et al.* 2021*a*). For
165 high Reynolds number turbulent flows, a recent study by Callaham *et al.* (2021*b*), the
166 statistical-state dynamics of turbulence in three-dimensional bluff-body wake was modelled
167 by combining a normal form amplitude equation with stochastic noise determined using a
168 similar sparse regression. This approach based on a simple normal form amplitude equation is,
169 however, not attractive for wall-bounded shear flows, as the key coherent structure dynamics
170 in this case involves a much more sophisticated global bifurcation (e.g. the crisis bifurcation;
171 see Kreilos & Eckhardt 2012) as well as a rich spatio-temporal dynamics that can be described
172 with the concept of thermodynamic phase transition (e.g. Avila *et al.* 2011; Barkley 2016).
173 It is finally worth mentioning that, in the context of turbulence modelling, there have been
174 several successful recent efforts made with the use of SINDy for a closure of the Reynolds-
175 Averaged Navier-Stokes (RANS) equations (e.g. Beetham & Capececiatro 2020; Schmelzer
176 *et al.* 2020; Beetham *et al.* 2021). A comprehensive review on the utilisation of machine
177 learning approaches for turbulence modelling in RANS and LES (large eddy simulation) can
178 also be found in Duraisamy (2021), where the need to augment the given turbulent model
179 using machine learning methods with suitable physical constraints was discussed.

1.3. Objective of the present study

180

181 The objective of the present study is to develop a reduced-order model more accurate than
 182 conventional ones for a turbulent state in wall-bounded shear flows. As the first step towards
 183 this task, we will consider a relatively simple but turbulent system: i.e. the minimal flow
 184 unit of a plane Couette flow (Hamilton *et al.* 1995), where the chaotic dynamics is well
 185 described in terms of the self-sustaining process. Based on the utilisation of POD modes,
 186 four different approaches will be considered and compared to devise a best performing
 187 reduced-order model: 1) Galerkin projection with a simple truncation; 2) sparse Galerkin
 188 regression (i.e. application of SINDy Brunton *et al.* 2016); 3) Galerkin projection with a
 189 simple eddy viscosity closure (Smith *et al.* 2005); 4) Galerkin projection with a SINDy
 190 closure for the truncation error. In particular, the last approach mentioned here is new and
 191 proposed by the present study, in which the concept of the optimal eddy viscosity (Protas
 192 *et al.* 2015) will be combined with a sparse regression. The idea of calibration of a given
 193 reduced-order model with an eddy-viscosity closure was previously proposed by several
 194 studies (e.g. Couplet *et al.* 2005; Cordier *et al.* 2010) with different types of regularisations.
 195 A similar idea was also recently explored in the recent work by Mohebujjaman *et al.* (2019),
 196 who applied a data-driven correction to a two-dimensional cylinder flow without an explicit
 197 physical closure model. In this context, it is worth mentioning that an important benefit of
 198 the l_1 -regularisation used in this study over the common l_2 -regularisation is that it prevents
 199 possible overfit of the eddy viscosity model which might yield an overdamped reduced-
 200 order model. The l_1 -regularisation will also offer a more parsimonious low-dimensional
 201 description. We will see that this approach enables us to effectively determine an ‘optimal’
 202 eddy viscosity, significantly improving the accuracy of the low-dimensional model based on
 203 POD modes.

204 This paper is organised as follows. In §2, the equations of motion, the flow geometry and
 205 the POD modes are introduced. The four reduced-order models are subsequently introduced
 206 and formulated in §3 and their performance will be examined and mutually compared in §4.
 207 This paper concludes in §5.

208 2. Background

209

2.1. Plane Couette Flow (PCF)

210 We consider a plane Couette flow (PCF) of an incompressible fluid, where the two walls
 211 move in opposite directions with the streamwise velocity, $\pm U_w$. The wall-normal distance
 212 between the two walls is given by $2h$. The kinematic viscosity of the fluid is ν , and the
 213 Reynolds number is defined by $Re = U_w h / \nu$. The streamwise, wall-normal and spanwise
 214 coordinates are made dimensionless with h , and they are denoted by $\mathbf{x} = (x, y, z)$. The two
 215 walls are set to be located at $y = \pm 1$. The equations of motion are then given by

$$216 \quad \frac{\partial \mathbf{u}}{\partial t} = -(\mathbf{u} \cdot \nabla) \mathbf{u} - y \frac{\partial \mathbf{u}}{\partial x} - \nu \mathbf{e}_x - \nabla p + \frac{1}{Re} \nabla^2 \mathbf{u}, \quad (2.1)$$

217 where t is the time, $\mathbf{u} = (u, v, w)$ is the perturbation velocity from the laminar base flow,
 218 $\mathbf{U} = (y, 0, 0)$, p the pressure and \mathbf{e}_x the unit vector in the streamwise direction.

219 To build a reduced-order model, we first perform a DNS confined to a minimal flow
 220 unit (MFU) (Jiménez & Moin 1991; Hamilton *et al.* 1995). Following Hamilton *et al.*
 221 (1995), the computational domain of $(L_x, L_y, L_z) = (1.75\pi, 2, 1.2\pi)$ is considered at
 222 $Re = 400$. The simulation was performed using `channelflow2.0`, an open-source DNS code
 223 (<https://www.channelflow.ch/>). The code uses the Fourier-Galerkin discretisation in the
 224 streamwise and spanwise directions and the Chebyshev-tau discretisation in the wall-normal

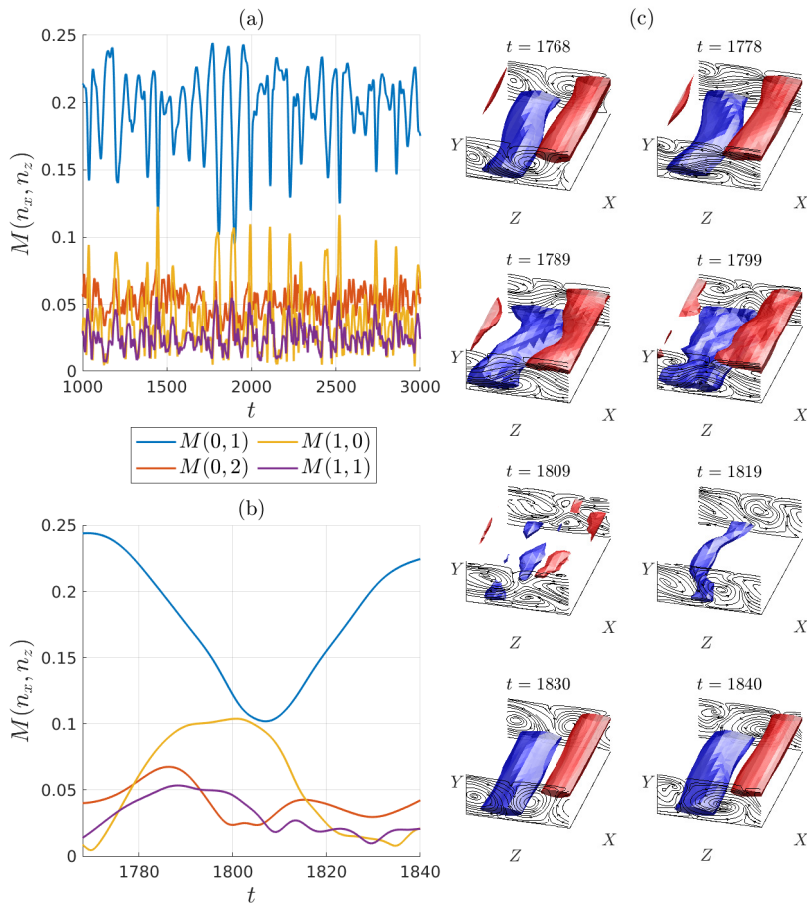


Figure 1: Time trace of $M(0, 1)$, $M(0, 2)$, $M(1, 0)$, $M(1, 1)$ (a) for $t = 1000 - 3000$ and (b) for $t = 1768 - 1840$. (c) Flow snapshots at $t = 1768, 1778, 1789, 1799, 1809, 1819, 1830, 1840$, where the blue and red iso-surfaces indicate $u = \pm 0.65$, respectively.

225 direction. The number of grid points in each spatial direction is given by $(N_x, N_y, N_z) =$
 226 $(16, 33, 16)$ (after dealiasing). A third-order semi-implicit backward difference formula
 227 (SDBF3) is used for the time-integration scheme. The simulation has been performed by
 228 setting a zero pressure gradient. The domain size normalised by viscous inner units (denoted
 229 by the superscript $(\cdot)^+$) is obtained as $(L_x^+, L_y^+, L_z^+) \simeq (186, 68, 127)$, in good agreement with
 230 that in Hamilton *et al.* (1995).

231 Figure 1 shows the DNS results, which exhibits the self-sustaining process (SSP). To
 232 examine the time evolution of the flow fields, the square root of energy of each plane Fourier
 233 mode is introduced:

$$234 \quad M(n_x, n_z) = \left(\int_{-1}^1 [\hat{u}^2(n_x, n_z, y) + \hat{v}^2(n_x, n_z, y) + \hat{w}^2(n_x, n_z, y)] dy \right)^{\frac{1}{2}}, \quad (2.2)$$

235 where $(\hat{\cdot})$ denotes the Fourier coefficients for the perturbation velocity, and n_x and n_z
 236 define the streamwise and spanwise wavenumbers such that $n_x \alpha$ and $n_z \beta$ ($\alpha = 2\pi/L_x$ and

237 $\beta = 2\pi/L_z$). Figure 1(a) shows the time trace featuring the quasi-periodic oscillation at the
 238 SSP time scale, $T_{SSP} \approx 80 - 90$. A sequence of flow field snapshots for a single SSP cycle,
 239 which correspond to the time trace in figure 1(b), are shown in figure 1(c). The initial flow
 240 field is featured with an amplified state of the high- and low-speed streamwise velocity streaks
 241 ($t = 1768$) (note that the time evolution of the streaks is depicted by $M(0, 1)$ in figure 1(b).
 242 The streaks subsequently become unstable (Hamilton *et al.* 1995) or experience the related
 243 transient growth (Schoppa & Hussain 2002), leading to their breakdown in a sinuously
 244 meandering manner. The streak breakdown emerges at $t = 1809$ where the streaks evidently
 245 disappear. Nonlinear processes subsequently regenerate streamwise vortices, leading to an
 246 increase in $M(1, 1)$. Finally, for $t = 1819 - 1840$, the regenerated streamwise vortices ($y - z$
 247 cut planes) redistribute the momentum from mean shear, resulting in the formation of new
 248 streaks especially near the lower wall region. This mechanism is known as the ‘lift-up’ effect.

249 2.2. Proper orthogonal decomposition

250 The proper orthogonal decomposition (POD) seeks a set of orthonormal functions that
 251 maximises the ensemble-averaged projection of the velocity perturbation, \mathbf{u} (e.g. Holmes
 252 *et al.* 1996). The optimisation is performed by solving the following eigenvalue problem:

$$253 \int_{\Omega} \langle \mathbf{u}(\mathbf{x}, t) \mathbf{u}^H(\mathbf{x}', t) \rangle \Phi_{n_x, n_z}^{(n)}(\mathbf{x}') d^3 \mathbf{x}' = \lambda_{n_x, n_z}^{(n)} \Phi_{n_x, n_z}^{(n)}(\mathbf{x}), \quad (2.3)$$

254 where $(\cdot)^H$ is the complex conjugate transpose, $\langle \cdot \rangle$ an ensemble average, $\lambda_{n_x, n_z}^{(n)}$ the
 255 eigenvalue representing the average kinetic energy contained in each POD mode and $\Phi_{n_x, n_z}^{(n)}$
 256 are the POD modes. Here, the eigenvalue and the corresponding POD modes are indexed by
 257 a positive integer n in decreasing order of the eigenvalue for each pair of the streamwise and
 258 spanwise wavenumber indices, (n_x, n_z) . The perturbation velocities are then represented in
 259 terms of a linear superposition of the POD modes:

$$260 \mathbf{u}(\mathbf{x}, t) = \sum_{n_x=-\infty}^{\infty} \sum_{n_z=-\infty}^{\infty} \sum_{n=1}^{\infty} a_{n_x, n_z}^{(n)}(t) \Phi_{n_x, n_z}^{(n)}(\mathbf{x}), \quad (2.4a)$$

261 where $a_{n_x, n_z}^{(n)}(t)$ is the time-dependent amplitude of each POD mode. Given the translational
 262 invariance in the streamwise and spanwise directions, Fourier expansions are *optimal* and
 263 the POD mode is further written as

$$264 \Phi_{n_x, n_z}^{(n)}(\mathbf{x}) = \frac{1}{\sqrt{L_x L_z}} e^{i(an_x x + \beta n_z z)} \phi_{n_x, n_z}^{(n)}(y), \quad (2.4b)$$

265 where $\phi_{n_x, n_z}^{(n)}(y)$ describes the wall-normal structure of each POD mode. Since the velocities
 266 in physical space are real-valued, the following conjugate symmetries are also satisfied:

$$267 a_{n_x, n_z}^{(n)}(t) = a_{-n_x, -n_z}^{(n)*}(t) \quad \text{and} \quad \Phi_{n_x, n_z}^{(n)} = \Phi_{-n_x, -n_z}^{(n)*}, \quad (2.4c)$$

268 where the superscript $(\cdot)^*$ indicates the complex conjugate. Substituting (2.4a) and (2.4b)
 269 into (2.3), the eigenvalue problem is simplified to

$$270 \int_{-1}^1 \underbrace{\langle \hat{\mathbf{u}}(n_x, n_z, y, t) \hat{\mathbf{u}}^H(n_x, n_z, y', t) \rangle}_{\equiv \hat{\mathbf{R}}} \phi_{n_x, n_z}^{(n)}(y') dy' = \lambda_{n_x, n_z}^{(n)} \phi_{n_x, n_z}^{(n)}(y). \quad (2.5)$$

271 The ensemble-averaged covariance $\hat{\mathbf{R}}$ is computed by enforcing the discrete symmetries

(n_x, n_z, n)	(0, 0, 1)	(0, ± 1 , 1)	(0, ± 2 , 1)	(± 1 , 0, 1)	(0, ± 3 , 1)	(0, 0, 2)	(0, ± 1 , 2)
λ	4.481	0.767	0.0574	0.0388	0.0201	0.0159	0.0113
E [%]	68.4	23.4	1.75	1.18	0.614	0.243	0.345

Table 1: Eigenvalues of the first 7 POD modes, ranked in terms of the eigenvalue of the POD mode λ . Here, E [%] is the total energy content of both (n_x, n_z, n) and $(-n_x, -n_z, n)$ wavenumber pairs.

273 of the PCF:

$$\begin{aligned}
\mathcal{I} &: [\mathbf{u}, \mathbf{v}, \mathbf{w}, p](x, y, z, t) = [\mathbf{u}, \mathbf{v}, \mathbf{w}, p](x, y, z, t), \\
\mathcal{P} &: [\mathbf{u}, \mathbf{v}, \mathbf{w}, p](x, y, z, t) = [-\mathbf{u}, -\mathbf{v}, -\mathbf{w}, p](-x, -y, -z, t), \\
\mathcal{R} &: [\mathbf{u}, \mathbf{v}, \mathbf{w}, p](x, y, z, t) = [\mathbf{u}, \mathbf{v}, -\mathbf{w}, p](x, y, -z, t), \\
\mathcal{RP} &: [\mathbf{u}, \mathbf{v}, \mathbf{w}, p](x, y, z, t) = [-\mathbf{u}, -\mathbf{v}, \mathbf{w}, p](-x, -y, z, t),
\end{aligned} \tag{2.6}$$

276 where \mathcal{I} is the identify transformation, \mathcal{P} , a point reflection about the origin, \mathcal{R} , a reflection
277 about the z -plane, and \mathcal{RP} , a 180° rotation about the z -axis. Given the statistically stationary
278 nature of the turbulent state and the invariance of the PCF under the discrete group
279 transformation in (2.6), the covariance operator is obtained as

$$\hat{\mathbf{R}}(n_x, n_z, y, y') = \frac{1}{4T} \int_{t_0}^{t_0+T} \sum_{\mathcal{T} \in \mathcal{D}_2} (\overline{\mathcal{T} : \mathbf{u}})(n_x, n_z, y, t) (\overline{\mathcal{T} : \mathbf{u}})^H(n_x, n_z, y', t) dt, \tag{2.7}$$

281 where $\mathcal{D}_2 = \{\mathcal{I}, \mathcal{P}, \mathcal{R}, \mathcal{RP}\}$.

282 For the computation of the POD modes, the ensemble-averaged covariance $\hat{\mathbf{R}}$ is first
283 obtained and the eigenvalue problem (2.5) is subsequently solved. Since the ensemble average
284 is equivalent to time average for a statistically stationary flow, $\hat{\mathbf{R}}$ is obtained by averaging in
285 time over an interval $t \in [-10000, 0]$ with a sampling time interval $\Delta t = 1$ (i.e. $t_0 = -10000$
286 and $T = 10000$). Within this time interval, the turbulent state is chosen to be statistically
287 stationary. We also note that the typical time period of the SSP is about $T_{SSP} \approx 80 - 90$,
288 implying that more than 100 cycles are considered for the construction of the POD modes.
289 Table 1 shows the leading eigenvalues obtained in the present study, and they are found to
290 match closely with those reported in Smith *et al.* (2005). The structures of the 9 leading POD
291 modes are also visualised in figure 2.

292 3. Reduced-order models

293 3.1. POD-Galerkin projection

294 To build a reduced-order model, we consider the velocity given by (2.4a) with a finite number
295 of POD modes:

$$\mathbf{u}(\mathbf{x}, t) = \sum_{n_x=-M_x}^{M_x} \sum_{n_z=-M_z}^{M_z} \sum_{n=1}^{N_p} a_{n_x, n_z}^{(n)}(t) \Phi_{n_x, n_z}^{(n)}(\mathbf{x}) + \mathbf{u}_R(\mathbf{x}, t), \tag{3.1}$$

297 where M_x , M_z and N_p are the numbers of streamwise, spanwise Fourier modes and $\phi_{n_x, n_z}^{(n)}$,
298 respectively. $\mathbf{u}_R(\mathbf{x}, t)$ is the residual velocity field that will not be resolved by the reduced-
299 order model. After substituting (3.1) into (2.1), the projection onto each POD basis yields
300 the following system of ordinary different equations (ODE):

$$\dot{\mathbf{a}} = \mathbf{L}\mathbf{a} + \mathbf{N}(\mathbf{a}, \mathbf{a}) + \mathbf{T}, \tag{3.2}$$

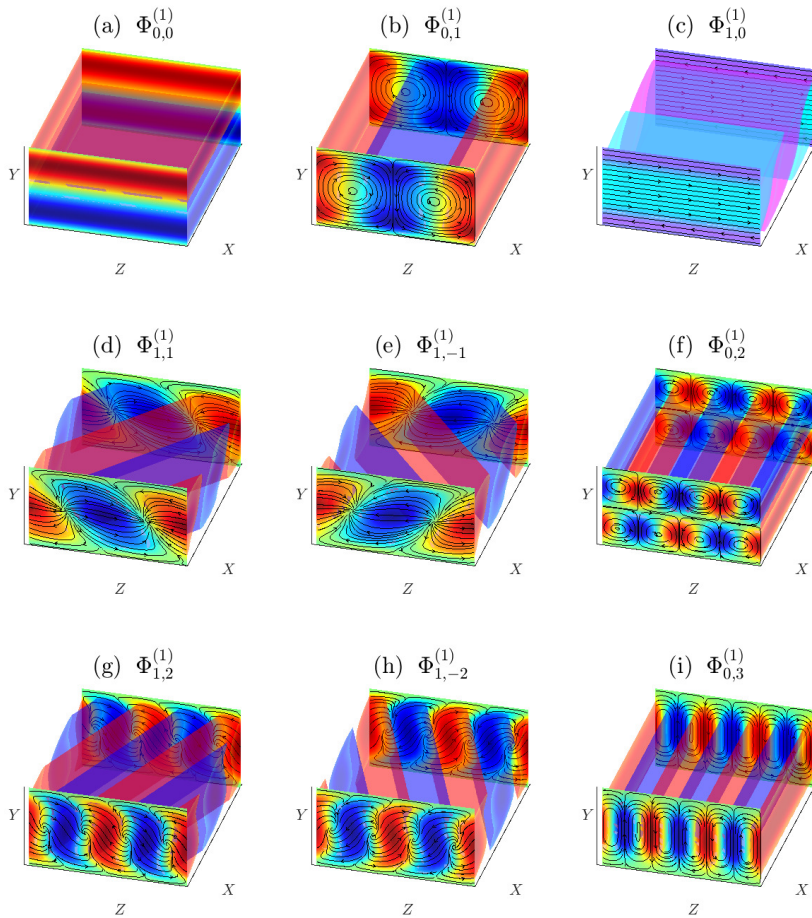


Figure 2: Visualisation of 9 leading POD modes (n_x, n_z, n) : (a) $(0, 0, 1)$; (b) $(0, 1, 1)$; (c) $(1, 0, 1)$; (d) $(1, 1, 1)$; (e) $(1, -1, 1)$; (f) $(0, 2, 1)$; (g) $(1, 2, 1)$; (h) $(1, -2, 1)$; (i) $(0, 3, 1)$. Iso-surfaces of (a,b,d-i) denote $u = -0.15$ (red) and $u = 0.15$ (blue). Iso-surfaces of (c) denote $w = 0.15$ (teal) and $w = -0.15$ (purple).

302 where $(\dot{\cdot}) \equiv d/dt$, $\mathbf{a} \in \mathbb{C}^r$ with $r = [(2M_x + 1)(2M_z + 1)N_p + 1]/2$ as the column vector,
 303 the element of which is given by $a_{n_x, n_z}^{(n)}$ for $-M_x \leq n_x \leq M_x$, $-M_z \leq n_z \leq M_z$ and
 304 $1 \leq n \leq N_p$, \mathbf{L} and \mathbf{N} are from the projection of the linear and quadratic nonlinear parts
 305 of (2.1) onto the finite number of POD modes (for further details on their definitions, see
 306 Appendix A), and \mathbf{T} is the residual term originating from $\mathbf{u}_R(\mathbf{x}, t)$. From (3.2), the simplest
 307 low-dimensional model is obtained by ignoring the residual term: i.e.

$$308 \quad \mathbf{T} = \mathbf{0}. \quad (3.3)$$

309 This case shall be referred to as the *POD-Galerkin model*.

3.2. Sparse POD-Galerkin regression

310

311 Several recent studies have proposed to identify \mathbf{L} and \mathbf{N} directly from the data (Brunton
 312 *et al.* 2016; Loiseau & Brunton 2018). If the dimension of the given nonlinear oscillation
 313 is sufficiently low (e.g. two-dimensional laminar cylinder wake), \mathbf{T} can be ignored with the
 314 use of a small number of POD modes. In this case, \mathbf{L} and \mathbf{N} can directly be obtained from
 315 the snapshots of \mathbf{a} using a sparse regression technique (i.e. SINDy; e.g. Brunton *et al.* 2016).
 316 SINDy is formulated by first collecting a set of time snapshots of the POD amplitudes from
 318 DNS (e.g. $\mathbf{a}_{dns}(t)$) into the following data matrices:

319
320

$$\mathbf{X} = [\mathbf{a}_{dns}(t_1) \quad \mathbf{a}_{dns}(t_2) \quad \dots \quad \mathbf{a}_{dns}(t_m)]^T, \quad (3.4a)$$

322 and

323
324

$$\dot{\mathbf{X}} = [\dot{\mathbf{a}}_{dns}(t_1) \quad \dot{\mathbf{a}}_{dns}(t_2) \quad \dots \quad \dot{\mathbf{a}}_{dns}(t_m)]^T. \quad (3.4b)$$

325

327

A set of candidate library functions, $\Theta(\mathbf{X})$, is subsequently constructed. In the present study,
 we restrict the library functions to be

328

$$\Theta(\mathbf{X}) = \begin{bmatrix} \mathbb{P}_{\mathbf{L}}(\mathbf{a}_{dns}(t_1)) & \mathbb{P}_{\mathbf{N}}(\mathbf{a}_{dns}(t_1)) \\ \mathbb{P}_{\mathbf{L}}(\mathbf{a}_{dns}(t_2)) & \mathbb{P}_{\mathbf{N}}(\mathbf{a}_{dns}(t_2)) \\ \vdots & \vdots \\ \mathbb{P}_{\mathbf{L}}(\mathbf{a}_{dns}(t_m)) & \mathbb{P}_{\mathbf{N}}(\mathbf{a}_{dns}(t_m)) \end{bmatrix}, \quad (3.5a)$$

329

330

332

where $\mathbb{P}_{\mathbf{L}}(\mathbf{X})$ and $\mathbb{P}_{\mathbf{N}}(\mathbf{X})$ denote the linear and quadratic combinations of the state vector
 admitted by the form of \mathbf{L} and \mathbf{N} in (3.2), respectively. We also introduce a coefficient matrix

333
334

$$\Xi = [\Xi_{\mathbf{L}} \quad \Xi_{\mathbf{N}}]^T, \quad (3.5b)$$

335

336

338

where $\Xi_{\mathbf{L}}$ and $\Xi_{\mathbf{N}}$ contain the (unknown) coefficients for $\mathbb{P}_{\mathbf{L}}(\mathbf{X})$ and $\mathbb{P}_{\mathbf{N}}(\mathbf{X})$. The coefficient
 matrix, Ξ , is subsequently determined by solving the following convex least squares
 regression problem:

339
340

$$\min_{\Xi} \|\dot{\mathbf{X}} - \Theta(\mathbf{X}) \Xi\|_2 + \gamma \|\Xi\|_1, \quad (3.6)$$

341

342

343

344

345

346

347

348

349

350

351

352

where $\|\cdot\|_2$ and $\|\cdot\|_1$ denote the standard ℓ_2 and ℓ_1 norms, respectively, and γ is the
 penalty introduced for the sparsity promoting ℓ_1 -regulariser. An advantage of using an ℓ_1 -
 regularisation compared to an ℓ_2 -regularisation is that they tend to prevent data overfit
 by promoting a model with the least complexity (sparse) required to model the dynamics
 (Brunton & Kutz 2019). The optimisation problem in (3.6) can be solved with the well-known
 LASSO (least absolute shrinkage and selection operator) algorithm. For large datasets, an
 alternative based on sequential threshold least squares was recommended instead – i.e. the
 SINDy approach (Brunton *et al.* 2016). This approach is used in the present study. We note
 that if the given dataset is even larger, the approach proposed by Gelb *et al.* (2019) may
 further be considered (i.e. multidimensional approximation of nonlinear dynamical systems
 (MANDy)). The sparse regression using a template given by the Galerkin projection will be
 referred to as the *POD-SINDy model*.

353

354

355

356

357

358

It is worth mentioning that the optimisation (3.6) was recently proposed to be solved with
 an equality constraint which explicitly enforces the energy conservation in the nonlinear
 operator \mathbf{N} (Loiseau & Brunton 2018): i.e. $\mathbf{a}^H \mathbf{N}(\mathbf{a}, \mathbf{a}) = 0$. However, this approach will not
 be considered in the present study, where the number of POD modes for the construction of
 a reduced-order model will not necessarily be large enough to fully cover the dimension of
 the given chaotic state. In such a case, the sparse regression in (3.6) implies that the residual

359 term \mathbf{T} in (3.2) is modelled as

$$360 \quad \mathbf{T} = \mathbf{L}_\Delta \mathbf{a} + \mathbf{N}_\Delta(\mathbf{a}, \mathbf{a}), \quad (3.7)$$

361 where \mathbf{L}_Δ and \mathbf{N}_Δ are the difference in \mathbf{L} and \mathbf{N} obtained by the Galerkin projection and the
 362 sparse regression. Therefore, the energy-conservation constraint for the nonlinear operator
 363 proposed by Loiseau & Brunton (2018) would enforce $\mathbf{a}^H(\mathbf{N}(\mathbf{a}, \mathbf{a}) + \mathbf{N}_\Delta(\mathbf{a}, \mathbf{a})) = 0$. However,
 364 this is not necessarily desirable in the present case, as will be discussed in the following
 365 subsection. Hence in §4.2, the library terms for the set of POD modes from the same
 366 wavenumber space, \mathbf{a}_{n_x, n_z} , are made dependent on the wavenumber of the POD modes as
 367 is suggestive from a Galerkin projection. The library function will consist of first-order
 368 polynomials of POD modes from the same wavenumber space. It attempts to model the \mathbf{L}_Δ
 369 terms of the dynamics. The modelling of the \mathbf{N}_Δ terms are accounted for by including the
 370 combination of POD modes that form a set of second-order polynomials which reflect the
 371 triadic wavenumber interactions, where $(n_x, n_z) = (k_x, k_z) + (m_x, m_z)$, from a POD-Galerkin
 372 model.

373 3.3. The needs for an eddy-viscosity closure

374 Now, we consider a physical model for \mathbf{T} . To rationalise the need of such a model, we first
 375 define \mathbf{a}_∞ as the solution to (3.2) for infinitely large M_x , M_z and N_p . In this case, the residual
 376 \mathbf{T} in (3.2) should vanish, thus \mathbf{a}_∞ would be identical to those obtained by projecting \mathbf{u} from
 377 DNS onto the POD modes. Given the energy-conserving nature of the nonlinear term in (2.1)
 378 (e.g. Joseph 1976), the contribution of the resulting nonlinear term to the change rate of the
 379 perturbation kinetic energy ($\mathbf{a}_\infty^H \mathbf{a}_\infty$) should be zero for every time instance, t , i.e.

$$380 \quad \mathbf{a}_\infty^H \mathbf{N}_\infty(\mathbf{a}_\infty, \mathbf{a}_\infty) = 0, \quad (3.8)$$

381 where \mathbf{N}_∞ is the quadratic nonlinear term obtained by considering infinitely large M_x , M_z and
 382 N_p . We note that (3.8) must also be true even if \mathbf{a}_∞ is replaced by any arbitrary vector. This
 383 observation motivated Loiseau & Brunton (2018) to impose $\mathbf{a}^H \mathbf{N}(\mathbf{a}, \mathbf{a}) = 0$ as an equality
 384 constraint into the optimisation problem in (3.6).

385 Let us now consider small values of M_x , M_z and N_p which define the size of the reduced-
 386 order model. In particular, we will assume that M_x , M_z and N_p are not large enough to
 387 cover the full energy cascade dynamics of the given turbulent state. We define a projection
 388 operator \mathcal{P}_l onto the subspace defined by the small values of M_x , M_z and N_p . Then, \mathbf{a}_∞
 389 can be decomposed into $\mathbf{a}_\infty = \mathbf{a}_{\infty, l} + \mathbf{a}_{\infty, h}$, where $\mathbf{a}_{\infty, l} = \mathcal{P}_l[\mathbf{a}_\infty]$ and $\mathbf{a}_{\infty, h} = \mathcal{P}_h[\mathbf{a}_\infty]$ with
 390 $\mathcal{I}_0[\cdot] = \mathcal{P}_l[\cdot] + \mathcal{P}_h[\cdot]$ ($\mathcal{I}_0[\cdot]$ is the identity operator). Using this decomposition and the
 391 quadratic nature of \mathbf{N}_∞ , (3.8) can be written as

$$392 \quad \mathbf{a}_{\infty, l}^H \left[\mathbf{N}_\infty(\mathbf{a}_{\infty, l}, \mathbf{a}_{\infty, h}) + \mathbf{N}_\infty(\mathbf{a}_{\infty, h}, \mathbf{a}_{\infty, l}) + \mathbf{N}_\infty(\mathbf{a}_{\infty, h}, \mathbf{a}_{\infty, h}) \right] \\ 393 \quad + \mathbf{a}_{\infty, h}^H \left[\mathbf{N}_\infty(\mathbf{a}_{\infty, l}, \mathbf{a}_{\infty, l}) + \mathbf{N}_\infty(\mathbf{a}_{\infty, l}, \mathbf{a}_{\infty, h}) + \mathbf{N}_\infty(\mathbf{a}_{\infty, h}, \mathbf{a}_{\infty, l}) \right] = 0, \quad (3.9)$$

394 where the top and bottom lines describe the nonlinear energy transport of the perturbation
 395 kinetic energy in the \mathcal{P}_l and \mathcal{P}_h subspaces, respectively. Here, we note that the term
 396 $\mathbf{a}_{\infty, l}^H \mathbf{N}_\infty(\mathbf{a}_{\infty, l}, \mathbf{a}_{\infty, l})$, equivalent to $\mathbf{a}^H \mathbf{N}(\mathbf{a}, \mathbf{a})$ expected from (3.2), vanishes due to (3.8), and
 397 so does $\mathbf{a}_{\infty, h}^H \mathbf{N}_\infty(\mathbf{a}_{\infty, h}, \mathbf{a}_{\infty, h})$ (note that the only difference between $\mathbf{a}_{\infty, l}^H \mathbf{N}_\infty(\mathbf{a}_{\infty, l}, \mathbf{a}_{\infty, l})$ and
 398 $\mathbf{a}^H \mathbf{N}(\mathbf{a}, \mathbf{a})$ are their dimension). The top line in (3.9) should indicate the rate of perturbation
 399 energy transferred from the \mathcal{P}_l to the \mathcal{P}_h subspace. Importantly, the energy cascade from
 400 large to small scales in the three-dimensional Navier-Stokes equations implies

$$401 \quad \left\langle \mathbf{a}_{\infty, l}^H \left[\mathbf{N}_\infty(\mathbf{a}_{\infty, l}, \mathbf{a}_{\infty, h}) + \mathbf{N}_\infty(\mathbf{a}_{\infty, h}, \mathbf{a}_{\infty, l}) + \mathbf{N}_\infty(\mathbf{a}_{\infty, h}, \mathbf{a}_{\infty, h}) \right] \right\rangle < 0 \quad (3.10a)$$

402 and

$$403 \quad \left\langle \mathbf{a}_{\infty,h}^H \left[\mathbf{N}_{\infty}(\mathbf{a}_{\infty,h}, \mathbf{a}_{\infty,h}) + \mathbf{N}_{\infty}(\mathbf{a}_{\infty,h}, \mathbf{a}_{\infty,l}) + \mathbf{N}_{\infty}(\mathbf{a}_{\infty,h}, \mathbf{a}_{\infty,h}) \right] \right\rangle > 0 \quad (3.10b)$$

404 for a statistically stationary flow where the ensemble average is equivalent to a time average.
 405 Indeed, this has been observed in a number of previous studies where the inter-scale energy
 406 transfer is analysed in detail (e.g. Cho *et al.* 2018; Lee & Moser 2019; Hwang & Lee 2020;
 407 Doohan *et al.* 2021b). Given the equivalence of $\mathbf{a}_{\infty,l}^H \mathbf{N}_{\infty}(\mathbf{a}_{\infty,l}, \mathbf{a}_{\infty,l})$ to $\mathbf{a}^H \mathbf{N}(\mathbf{a}, \mathbf{a})$, a condition
 408 for \mathbf{T} to meet from a physical viewpoint would then be

$$409 \quad \langle \mathbf{a}^H \mathbf{T} \rangle < 0, \quad (3.11)$$

410 indicating that the residual term, \mathbf{T} , in (3.2) must contain an energy-removal mechanism.

411 The discussion above evidently justifies the use of an eddy viscosity model in many
 412 previous studies (e.g. Aubry *et al.* 1988; Rempfer & Fasel 1994a,b; Smith *et al.* 2005; Östh
 413 *et al.* 2014; Protas *et al.* 2015): i.e.

$$414 \quad \mathbf{T} = \nu_t \mathbf{D} \mathbf{a}, \quad (3.12)$$

415 where ν_t is a scalar-valued eddy viscosity and \mathbf{D} is the Laplacian operator for the reduced-
 416 order model defined in Appendix A. For $\nu_t > 0$, (3.12) yields a sufficient condition for
 417 (3.11), as it ensures $\mathbf{a}^H \mathbf{T} (= \nu_t \mathbf{a}^H \mathbf{D}) \mathbf{a} < 0$ at every time for non-zero \mathbf{a} with $(n_x, n_z) \neq (0, 0)$
 418 due to the negative semi-definite nature of \mathbf{D} (see Appendix A). In the previous studies,
 419 various form of eddy viscosity have been introduced and examined. In the present study,
 420 we will first consider a simple spectral eddy viscosity model similar to the one in Smith
 421 *et al.* (2005) where an empirical real-valued constant of ν_t is employed. It is evident that
 422 the performance of this simple single-valued eddy viscosity model is expected to be limited,
 423 as there is evidence supporting the complex nature of the inter-modal energy transfer (e.g.
 424 Couplet *et al.* 2003; Podvin 2009, see also §4.3). Therefore, this approach here is considered
 425 for the purpose of comparing with the other models. This approach shall be referred to as
 426 *POD-Galerkin-E model* (the ‘E’ stands for an ‘empirical’ eddy viscosity).

427 3.4. Sparse optimal eddy-viscosity closure

428 Although the eddy viscosity model in (3.12) ensures the physical property that originates
 429 from the energy cascade of turbulent state, (3.11), it is evidently too crude. Indeed, $\mathbf{a}^H \mathbf{T}$ does
 430 not have to be negative for every point in time like the one ensured by (3.12) – only its time
 431 average needs to be negative. Furthermore, there is no physical reason that different POD
 432 modes should feel the ‘same’ eddy viscosity: for example, the POD modes for large n_x , n_z
 433 and n are not expected to experience a large amount of energy removal from their dynamics
 434 by \mathbf{T} . More flexible forms of eddy viscosity have therefore been proposed previously (for a
 435 review, see Östh *et al.* 2014, where various forms of eddy viscosity have been examined for a
 436 three-dimensional turbulent bluff-body wake). In particular, Protas *et al.* (2015) introduced
 437 the concept of ‘optimal’ eddy viscosity by formulating an adjoint-based optimisation problem
 438 that minimises the difference between the POD amplitudes from the measurement and the
 439 reduced-order model. However, as discussed in §1, the application of the adjoint-based
 440 optimisation to a turbulent flow does not always allow for a sufficient long optimisation time
 441 interval due to the unstable nature of the adjoint system around a chaotic state. Also, the
 442 approach of Protas *et al.* (2015) is still based on a scalar-valued eddy viscosity, although its
 443 generalisation to a sophisticated form of eddy viscosity is easily possible.

444 In the present study, we take an alternative formulation which enables us to consider a long
 445 time horizon for a similar optimisation problem. In particular, we determine an optimal eddy
 446 viscosity with the sparse regression in §3.2. For the demonstrative purpose, we consider a
 447 nonlinear closure model for \mathbf{T} (Östh *et al.* 2014; Protas *et al.* 2015), in which a complex-valued

448 eddy viscosity is set to vary with POD modes:

$$449 \quad \mathbf{T} = \mathbf{V}_t \mathbf{D} \mathbf{a} \quad (3.13a)$$

450 with

$$451 \quad \mathbf{V}_t(t) = e(t) \text{diag}[\mathbf{c}], \quad (3.13b)$$

452 where $e(t)$ is a scalar-valued function of \mathbf{a} that can be chosen for a nonlinear eddy viscosity
 453 model and \mathbf{c} the constant vector to be determined for each n_x, n_z and n . We note that the
 454 choice of e usually ensures \mathbf{V}_t to vanish as \mathbf{a} becomes zero. In previous studies (e.g. Östh
 455 *et al.* 2014; Protas *et al.* 2015), the perturbation kinetic energy, $e(t) = (\mathbf{a}^H \mathbf{a})^{1/2}$, has often
 456 been considered. In the present study, a simpler form, $e(t) = |a_{0,0}^{(1)}|$, is chosen, given that the
 457 corresponding mode contains approximately 70% of the total perturbation kinetic energy (see
 458 table 1). A preliminary test also reveals that this choice makes the optimised reduced-order
 459 model perform slightly better than that of $e(t) = (\mathbf{a}^H \mathbf{a})^{1/2}$ (see Appendix B).

460 Now, we formulate an optimisation problem determining \mathbf{V}_t in (3.13b). Using the POD
 461 mode amplitudes obtained from DNS (i.e. \mathbf{a}_{dns}) and (3.2), the desired residual term of the
 462 low-dimensional system is given by

$$463 \quad \mathbf{T}_{dns}(t) \equiv \dot{\mathbf{a}}_{dns}(t) - \mathbf{L} \mathbf{a}_{dns} - \mathbf{N}(\mathbf{a}_{dns}, \mathbf{a}_{dns}), \quad (3.14)$$

464 where \mathbf{T}_{dns} indicates the residual term calculated with \mathbf{a}_{dns} . Similarly to the sparse regression
 466 in §3.2, a set of time snapshots of $\mathbf{T}_{dns}(t)$ is introduced into a data matrix using (3.14):

$$467 \quad \mathbf{Y} = [\mathbf{T}_{dns}(t_1) \quad \mathbf{T}_{dns}(t_2) \quad \dots \quad \mathbf{T}_{dns}(t_m)]^T. \quad (3.15a)$$

470 Given (3.13a), the related library function for the optimisation is subsequently formed to be

$$471 \quad \Theta_e(\mathbf{Y}) = [e_{dns}(t_1) \mathbf{a}_{dns}(t_1) \mathbf{D} \quad e_{dns}(t_2) \mathbf{a}_{dns}(t_2) \mathbf{D} \quad \dots \quad e_{dns}(t_m) \mathbf{a}_{dns}(t_m) \mathbf{D}]^T, \quad (3.15b)$$

473 where $e_{dns}(t)$ is e obtained from DNS. Since we seek a complex-valued constant vector \mathbf{c}
 474 that minimises the difference between \mathbf{T}_{dns} given by (3.14) and \mathbf{T} from the residual model
 476 in (3.13a), the following optimisation is defined:

$$477 \quad \min_{\mathbf{c}} \|\mathbf{Y} - \Theta_e(\mathbf{Y}) \text{diag}[\mathbf{c}]\|_2 + \gamma_e \|\mathbf{c}\|_1, \quad (3.16)$$

479 where γ_e is the parameter for the sparsity-promoting ℓ_1 -regulariser. Like the optimisation
 480 problem in (3.6), (3.16) is solved by applying the SINDy approach (Brunton *et al.* 2016). This
 481 approach will be referred to as *POD-Galerkin-R model* (the ‘R’ stands the determination of an
 482 eddy viscosity with a sparse ‘regression’). As mentioned in §1, several previous studies (e.g.
 483 Couplet *et al.* 2005; Cordier *et al.* 2010) proposed a similar idea of calibrating the residual
 484 term, \mathbf{T} , using Tikhonov regularisation, an optimisation based on the ℓ_2 -regularisation. Here,
 485 the ℓ_1 -regularisation has a benefit over the ℓ_2 -regularisation, as it is designed to prevent data
 486 overfit, offering a parsimonious low-dimensional model. Lastly, we note that setting $\gamma_e \rightarrow \infty$
 487 results in the POD-Galerkin model, while $\gamma_e \rightarrow 0$ yields the least-square eddy viscosity (for
 488 a further discussion on the effect of γ_e , see Appendix C).

489 It is also useful to make some remarks on the least-square sparse regression in (3.16).
 490 First, the regression (3.16) can now consider a very long sampling time, as it simply relies on
 491 the POD mode amplitudes, \mathbf{a}_{dns} , taken from DNS. Therefore, it no longer suffers from the
 492 finite optimisation time-interval issue that one may face in the conventional adjoint-based
 493 formulation. Second, the regression problem (3.16) can flexibly be formulated by accounting
 494 for various forms of eddy viscosity, and this can be achieved by adding more library functions
 495 in (3.15b). Third, the regression (3.16) allows for negative elements of \mathbf{V}_t (or \mathbf{c}), indicating
 496 that the ‘backwards scattering’ in the energy cascade can be taken into account. Although

Model	Physics	Model for \mathbf{T}	Technique for \mathbf{T}
POD-Galerkin	-	$\mathbf{0}$	-
POD-SINDy	-	$\mathbf{L}_\Delta \mathbf{a} + \mathbf{N}_\Delta(\mathbf{a}, \mathbf{a})$	Sparse Regression
POD-Galerkin-E	Energy Cascade	$\mathbf{v}_t^T \mathbf{D} \mathbf{a}$	Empirical
POD-Galerkin-R	Energy Cascade	$\mathbf{V}_t^T \mathbf{D} \mathbf{a}$	Sparse Regression

Table 2: Summary of the reduced-order models.

497 this issue may cause a potential numerical instability of the resulting reduced-order model,
 498 it may well be fixed by imposing an additional inequality constraint (e.g. all the element
 499 of \mathbf{c} is greater than or equal to zero). Finally, \mathbf{V}_t (or \mathbf{c}) in (3.13b) can also be a complex
 500 vector, given that \mathbf{a} is complex. In other words, some ‘dispersive’ effect in the dynamics of
 501 the reduced-order model can also be added with non-zero imaginary part of \mathbf{V}_t .

502 4. Results and discussions

503 We examine the reduced-order models obtained by applying the approaches in §3 to the PCF
 504 introduced in §2. In table 2, the extent that each model utilises physical information and data
 505 from DNS is summarised with the form of the closure. The approach relying on the data
 506 most is the POD-SINDy model, as it determines all the elements of the operator \mathbf{L}_Δ and
 507 \mathbf{N}_Δ by solving the regression problem in (3.6). On the other hand, the approach accounting
 508 for both physics and data to the largest extent would be the POD-Galerkin-R model, as a
 509 physics-informed and flexible form of \mathbf{T} is determined in a data-driven manner.

510 4.1. Dimension of the reduced-order model: POD-Galerkin model

511 The POD-Galerkin model introduced in §3.1 is first studied to determine a few reference
 512 reduced-order models. For simplicity, only the most energetic POD mode is taken for each
 513 n_x and n_z , and the dimension of the reduced-order model is varied with the number
 514 of the plane Fourier modes. Three different cases are considered: i) 6-modes with $\mathbf{a} =$
 515 $[a_{0,0}^{(1)}, a_{0,\pm 1}^{(1)}, a_{0,\pm 2}^{(1)}, a_{\pm 1,0}^{(1)}, a_{\pm 1,\pm 1}^{(1)}, a_{\pm 1,\mp 1}^{(1)}]$ examined in Smith *et al.* (2005); ii) 25-modes with
 516 $\mathbf{n}(\equiv [N_p, M_x, M_z]) = [1, 3, 3]$ (see (3.1)); iii) 41-modes with $\mathbf{n} = [1, 4, 4]$. Figure 3 shows
 517 the time trace of the Fourier-mode energy, $M(n_x, n_z)$, for the three cases. In all cases, the
 518 initial condition for \mathbf{a} is obtained by projecting a DNS field onto the corresponding POD
 519 mode subspace. For the 6-mode case, the state vector, \mathbf{a} , reaches a non-trivial equilibrium
 520 state after an oscillatory transient, consistent with the result of Smith *et al.* (2005) (figure
 521 3a). Given that the 6-mode model exhibits a stable non-trivial equilibrium (i.e. $\mathbf{a} \neq \mathbf{0}$), this
 522 would not be a good reference case to build a low-dimensional model exhibiting chaotic
 523 dynamics. Considering a larger number of plane Fourier modes (i.e. 25- and 41-modes),
 524 the state vector, \mathbf{a} , of the reduced-order model exhibits a chaotic trajectory (figures 3b,c).
 525 However, the values of $M(n_x, n_z)$ appear to be far off from those in DNS. In particular, the
 526 second most energetic mode of the POD-Galerkin model, $M(0, 1)$, which would represent the
 527 time evolution of streaks, significantly deviates from DNS. Despite this issue, the presence
 528 of the chaotic dynamics in the POD-Galerkin models with 25- and 41-modes indicates that
 529 they would be good reference cases which the other modelling approaches in §3 can further
 530 be employed. Therefore, the remaining part of the present study will only consider the 25-
 531 and 41-mode cases.

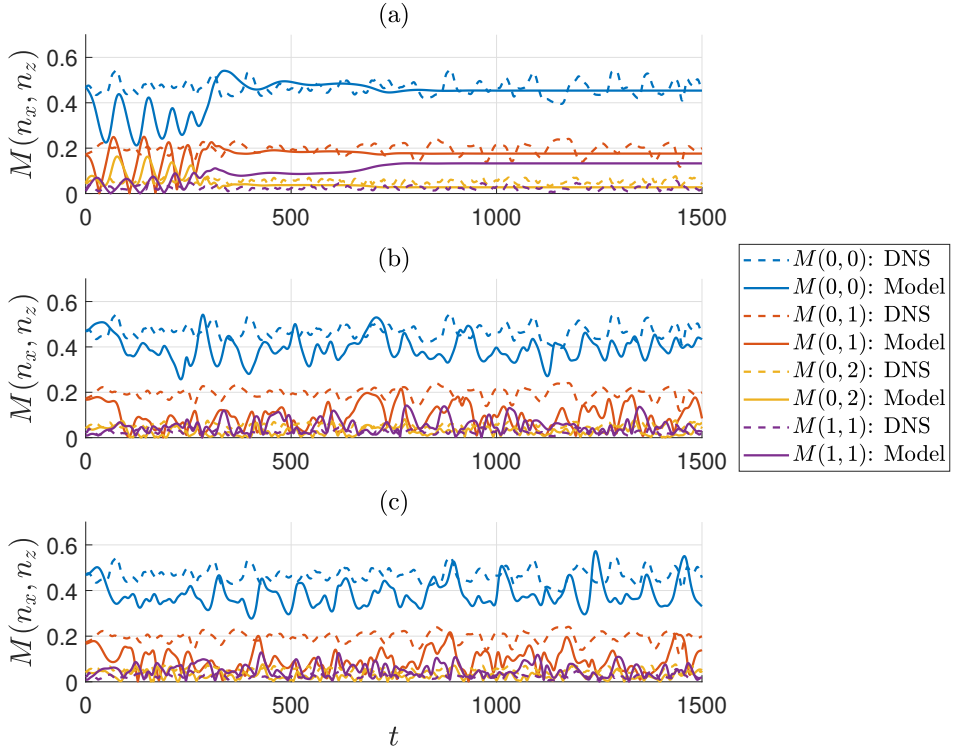


Figure 3: Time trace of $M(n_x, n_z)$ of the POD-Galerkin model: (a) 6 modes (Smith *et al.* 2005); (b) 25 modes; (c) 41 modes.

532

4.2. Sparse POD-Galerkin regression: POD-SINDy model

533 Based on the 25- and 41-mode cases in §4.1, the optimisation problem in (3.6) is solved for
 534 $t \in [-10000, 0]$ with an sampling interval of $\Delta t = 0.5$, in order to obtain the corresponding
 535 POD-SINDy model. The model constructed is subsequently examined by considering an
 536 additional time interval $t \in [0, 5000]$. The relative error of the least-squares regression
 537 defined in (3.6) is reported in table 3 for the 25-mode model. Here, the relative error is
 538 defined as

$$539 \quad \mathcal{E}_{PS} = \frac{1}{N_{\text{mode}}} \sum_{n_x=-M_x}^{M_x} \sum_{n_z=-M_z}^{M_z} \sum_{n=1}^{N_p} \frac{\|[\dot{\mathbf{X}} - \Theta(\mathbf{X})\Xi]_{n_x, n_z}^{(n)}\|_2}{\|[\dot{\mathbf{X}}]_{n_x, n_z}^{(n)}\|_2}, \quad (4.1)$$

540 where $[\cdot]_{n_x, n_z}^{(n)}$ indicates the component defined by the POD mode indices given in (2.4a).
 541 N_{mode} is defined as the number of POD modes used in the sparse regression. We note that
 542 the relative error is normalised by N_{mode} such that $\mathcal{E}_{PS} \in [0, 1]$. As expected, the relative
 543 error reaches the minimum when γ is zero (least-squares regression). When γ is increased,
 544 the relative error becomes larger due to the increased sparsification penalty as defined in
 545 equation (3.6).

546 The 6-mode POD-SINDy model obtained and the 25-mode POD-SINDy model obtained
 547 in this way is subsequently simulated. It is found that the POD-SINDy model rapidly blows up
 548 for $t \in [0, 4]$, and this behaviour remains unchanged for relatively low values of $\gamma \in [0, 0.1]$.
 549 For $\gamma = 1$, only $M(0, 2)$ blows up while the rest remains relatively stable, although all the

γ	0	0.0001	0.001	0.01	0.1	1	10
\mathcal{E}_{PS} (training)	0.69	0.69	0.69	0.69	0.75	0.98	0.99
\mathcal{E}_{PS} (validation)	0.68	0.68	0.68	0.68	0.73	0.98	0.99
$N_0(\mathbf{L})$	0	0	0	0	31	49	49
$N_0(\mathbf{N})$	0	0	0	2	78	534	664

Table 3: Relative error of the least-squares regression in (3.6) for the POD-SINDy model with 25-modes. Here, \mathcal{E}_{PS} is defined in (4.1), which is the summation of the relative error of each mode when compared to DNS data, normalised by the total number of POD modes. The ‘training’ and ‘validation’ in second and third lines imply \mathcal{E}_{PS} from $t \in [-10000, 0]$ and $t \in [0, 5000]$, respectively. Also, $N_0(\cdot)$ indicates the number of zero terms in the linear operator \mathbf{L} and in the nonlinear operator \mathbf{N} , except the Reynolds shear-stress term in the mean equation, in the model. Note that the number of the POD modes used for the 25-mode POD-SINDy model is $N_{\text{mode}} = 49$ due to the conjugate symmetry (i.e. 1 mode for the mean equation and 2×24 modes for the fluctuation equations).

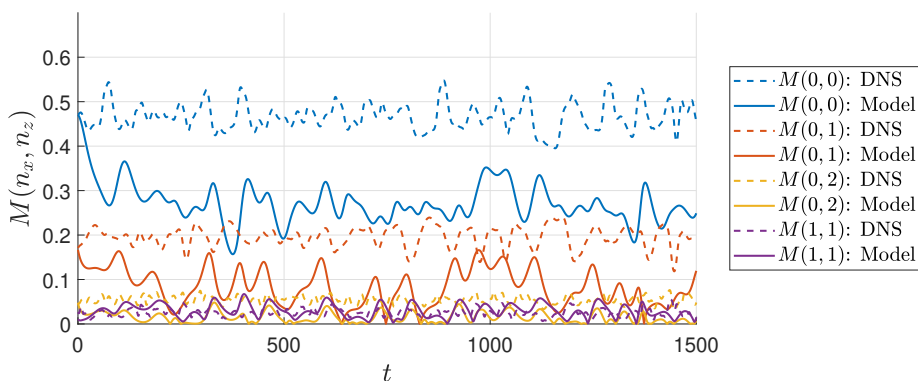


Figure 4: Time trace of $M(n_x, n_z)$ from DNS and the POD-Galerkin-E model with 25 modes ($\nu_t = 0.003$).

550 linear terms are zero in this case (see table 3). For $\gamma = 10$, all the terms in the regression
551 from the GP-template are zero, except for the nonlinear terms for the equation for $\hat{a}_{0,0}^{(1)}$. The
552 application of this approach to the 41-mode case also exhibits a similar behaviour, thus it is
553 not pursued any more. The blow-up of the POD-SINDy model was not reported in previous
554 studies (e.g. Brunton *et al.* 2016; Loiseau & Brunton 2018; Rubini *et al.* 2021). However, it
555 is worth mentioning that the dimension of nonlinear oscillations in such cases are low (e.g.
556 Lorenz chaos, two-dimensional laminar vortex shedding, and two-dimensional cavity flows).
557 As such, the number of POD modes considered in those studies appear to be large enough
558 to cover the full nonlinear dynamics using sparse regression. This suggests that the blow-up
559 of the POD-SINDy model shown here are presumably caused by the number of POD modes
560 that is not large enough to cover the full chaotic dynamics of interest. As discussed in §3.2,
561 in this case, the POD-SINDy model takes the residual term \mathbf{T} in the form of (3.7), which
562 does not necessarily ensure (3.11).

γ_e	0.0003	0.0005	0.001	0.005	0.1
\mathcal{E}_{PGR} (training)	0.93	0.93	0.96	1	1
\mathcal{E}_{PGR} (validation)	0.92	0.92	0.95	1	1
N_0	11	15	35	49	49

Table 4: Relative error of the least-squares regression in (3.16) for the POD-Galerkin-R model with 25 modes. Here, \mathcal{E}_{PGR} is defined in (4.2). The ‘training’ and ‘validation’ in second and third lines imply \mathcal{E}_{PS} from $t \in [-10000, 0]$ and $t \in [0, 5000]$, respectively. As in Table 3, N_0 indicates the number of zero valued eddy-viscosity terms for $N_{\text{mode}} = 49$.

563

4.3. Utilisation of an empirical eddy viscosity: POD-Galerkin-E model

564 The POD-Galerkin-E model, which utilises the simple spectral eddy viscosity of Smith
565 *et al.* (2005), is examined by considering a few values of ν_t defined in (3.12): $\nu_t =$
566 $(0.001, 0.003, 0.005)$. It is, however, found that the introduction of such a simple eddy
567 viscosity closure does not significantly improve the accuracy of the reduced-order model
568 compared to the original POD-Galerkin model. Indeed, $\nu_t = 0.001$ is found to be too small
569 to influence the original POD-Galerkin model, while $\nu_t = 0.005$ is too large and stabilises
570 the chaotic dynamics into a stable non-trivial equilibrium. Here, we present the results for
571 $\nu_t = 0.003$, which was determined by accounting for this observation like Smith *et al.*
572 (2005). Figure 4 compares the time trace of $M(n_x, n_z)$ from DNS with that from the POD-
573 Galerkin-E model with 25-modes for $\nu_t = 0.003$. The mean component, $M(0, 0)$, which
574 contains the largest perturbation energy, exhibits a large difference from that of DNS. In
575 fact, this deviation is greater than that of the POD-Galerkin model which does not employ
576 any model of \mathbf{T} (compare figure 4 with figure 3b). However, it should be mentioned that not
577 all of the mode amplitudes exhibit such a deterioration. The POD-Galerkin-E model is also
578 found to exhibit a much more improved $M(1, 1)$ (compare figure 4 with figure 3b; see also
579 table 5), indicating that the utilisation of a suitable eddy viscosity closure would improve the
580 performance of a reduced-order model. This will be seen in §4.5.

581

4.4. Sparse optimal closure: POD-Galerkin-R model

582 We now consider the POD-Galerkin-R model where a flexible form of eddy viscosity is
583 determined by solving the least-squares regression problem in (3.16). The regression is
584 performed with the data taken for $t \in [-10000, 0]$ with an sampling interval of $\Delta t = 0.5$, and
585 the model is subsequently examined by considering an additional time interval $t \in [0, 5000]$.
586 Similarly to (4.2), the relative error of the regression is defined as

$$587 \quad \mathcal{E}_{PGR} = \frac{1}{N_{\text{mode}} - 1} \sum_{n_x=-M_x}^{M_x} \sum_{n_z=-M_z}^{M_z} \sum_{n=1}^{N_p} \frac{\|[\mathbf{Y} - \Theta_e(\mathbf{Y}) \text{diag}[\mathbf{c}]]_{n_x, n_z}^{(n)}\|_2}{\|[\mathbf{Y}]_{n_x, n_z}^{(n)}\|_2} \quad (4.2)$$

588 for $(n_x, n_z) \neq (0, 0)$, and it is reported in table 4 for the 25-mode model. Note that the
589 mode with $(n_x, n_z) = (0, 0)$ is excluded from the relative error statistics as no residual
590 term was applied to this mode. As expected, the relative error becomes larger as the ℓ_1 -
591 regularisation penalty, γ_e , increases. For $\gamma_e > 0.005$, \mathcal{E}_{PGR} remains unchanged, indicating
592 that the regression would not make any improvement. In the present study, we have chosen
593 to present the result for $\gamma_e = 0.0005$ which renders the proposed regression sufficiently
594 effective, while not allowing for too small values in \mathbf{c} that could well be from some numerical
595 issues (e.g. sampling time interval). We also ensure that our residual model does not overfit

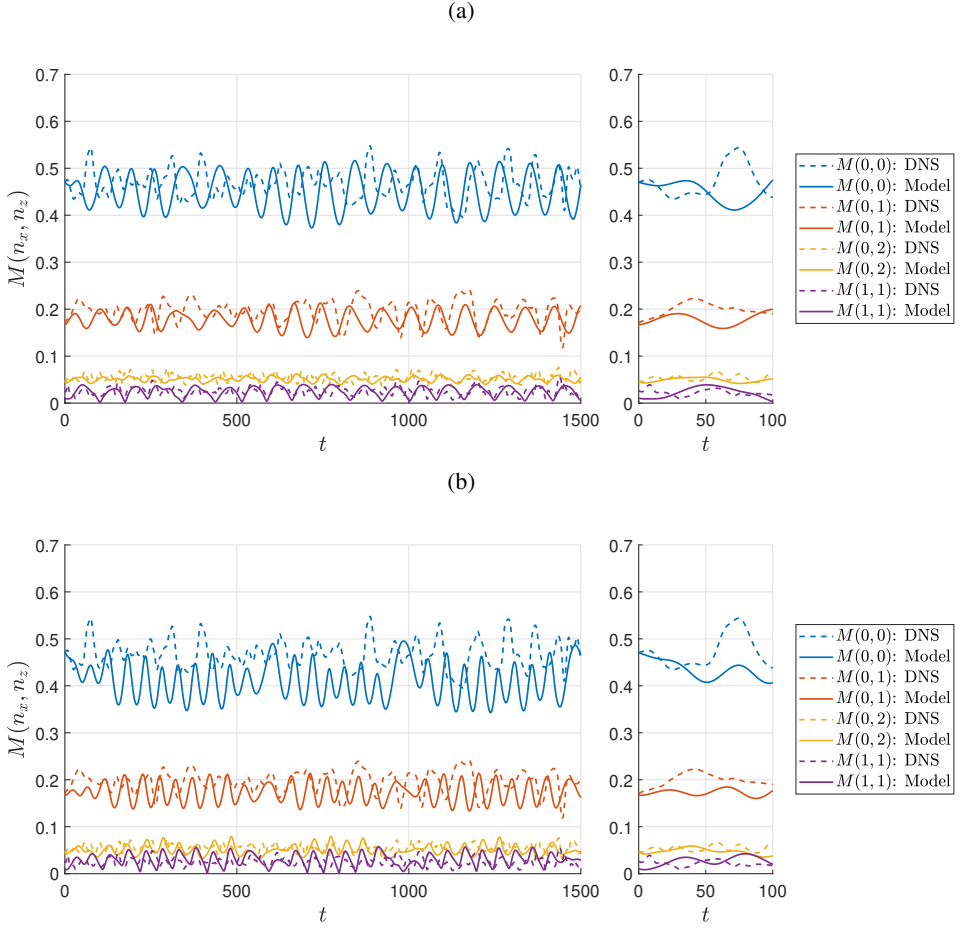


Figure 5: Time trace of $M(n_x, n_z)$ from DNS and the POD-Galerkin-R model: (a) 25-modes ($\gamma_e = 0.0005$); (b) 41-modes ($\gamma_e = 0.0001$). The misalignment of the initial condition at $t = 0$ for $M(1, 1)$ between the model and DNS data are due to the residual flow-field not being capture by the POD basis.

596 our training dataset by comparing the training and validation set error quantitatively as seen
597 in table 4.

598 Figure 5 shows time trace of $M(n_x, n_z)$ from the POD-Galerkin-R model utilising 25- and
599 41-modes, and it is compared with that from DNS. The time traces of $M(n_x, n_z)$ from the
600 POD-Galerkin-R model are now quite close to those from DNS, including the initial time
601 evolution of the three most energetic modes ($M(0, 0)$, $M(0, 1)$ and $M(0, 2)$ for $t < 50$) –
602 note that the Lyapunov time would be expected to be at the order of the smallest time scale
603 of the flow (i.e. the Kolmogorov time scale), which is given by $t \sim O(10)$ in the present case
604 (e.g. Ruelle 1979; Crisanti *et al.* 1993). This indicates that the performance of this model is
605 evidently far superior to that of the POD-Galerkin and the POD-Galerkin-E models. Both of
606 the 25- and 41-mode cases of the POD-Galerkin-R model also exhibit a chaotic oscillation
607 with the time scale close to that of DNS, observed in figure 8, and which will be discussed
608 in §4.5.

609 The constant vector $\mathbf{c}(=c_{n_x, n_z}^{(n)})$ used for the eddy viscosity in (3.13b) is also visualised
610 in figure 6. We first consider the 25-mode case (figure 6a). Here, we note that the constant

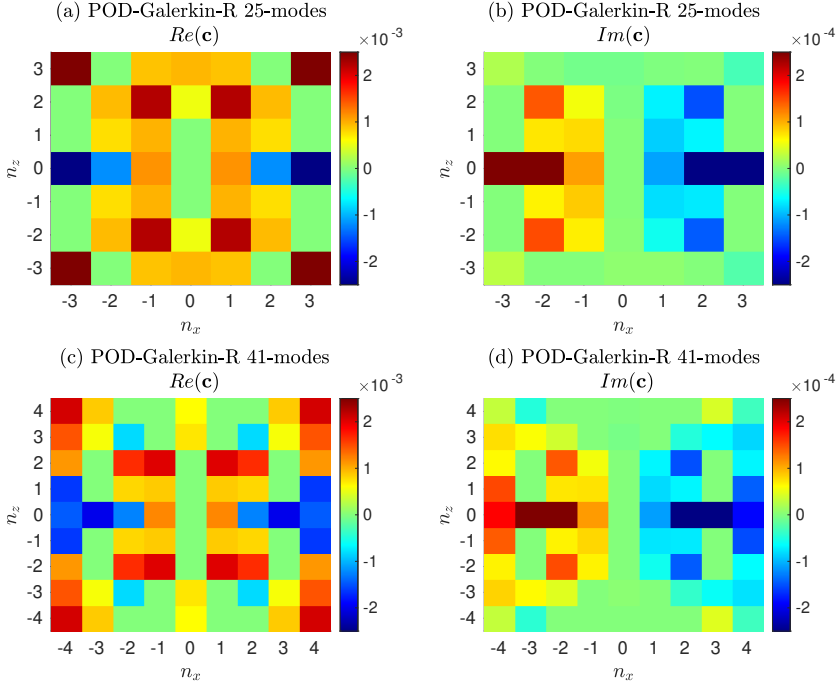


Figure 6: Distribution of real (left column) and imaginary (right column) part of $c_{n_x, n_z}^{(n)}$ in the $n_x - n_z$ plane : (a,b) 25-modes ($\gamma_e = 0.0005$); (c,d) 41-modes ($\gamma_e = 0.0001$).

611 vector, \mathbf{c} , exhibits a conjugate symmetry because the velocity in this study is real-valued.
 612 It also appears to be distributed highly symmetrically in the $n_x - n_z$ plane. This originates
 613 from the \mathcal{R} symmetry in (2.6) – the \mathcal{R} symmetry imposes the streamwise and wall-normal
 614 components of $\phi_{n_x, n_z}^{(n)}$ and $\phi_{n_x, -n_z}^{(n)}$ to be identical and their spanwise component to have the
 615 opposite signs, while the energy of the streamwise component dominates over the other two
 616 components (see also figure 7). The real part of \mathbf{c} , proportional to the strength of dissipation
 617 (i.e. the removal of the energy from the given dynamics), is positive for most pairs of
 618 (n_x, n_z) in the $n_x - n_z$ plane, as expected from (3.11). However, there are some $c_{n_x, n_z}^{(n)}$
 619 which exhibit negative values, and this is particularly pronounced around $(n_x, n_z) = (\pm 3, 0)$. This
 620 indicates that allowing for negative elements of \mathbf{c} does help to improve the performance
 621 of the reduced-order model as discussed in §3.4. It is interesting to note that the higher
 622 streamwise and spanwise independent modes are energised (inverse energy transfer) and
 623 dissipated (forward energy cascade) respectively, consistent with the findings from Podvin
 624 (2009). Furthermore, some $c_{n_x, n_z}^{(n)}$ also exhibit non-zero imaginary values. However, their
 625 amplitudes are overall an order-of-magnitude smaller than those of the real counter part,
 626 implying that the dispersive effect imposed by the imaginary part of $c_{n_x, n_z}^{(n)}$ would not be
 627 significant. Finally, the distribution of $c_{n_x, n_z}^{(n)}$ for the 41-mode case (figures 6c,d) shows that
 628 increasing the number of POD modes do not significantly change the overall distribution and
 629 strength of $c_{n_x, n_z}^{(n)}$ in the $n_x - n_z$ plane (compare figures 6a,b with 6c,d). We note that as the
 630 number of POD modes is increased, the eddy viscosity also needs to vanish. However, this is
 631 not observed in figure 6. Instead, the similar distribution of $c_{n_x, n_z}^{(n)}$ for the 25- and 41-mode
 632 cases suggests that the eddy viscosity obtained with (3.16) is coherently compensating for

Cases	# of POD modes	$\langle a_{0,0}^{(1)} \rangle$	$\langle a_{0,1}^{(1)} \rangle$	$\langle a_{0,2}^{(1)} \rangle$	$\langle a_{1,1}^{(1)} \rangle$
DNS	N/A	2.110	0.881	0.230	0.079
POD-Galerkin	25	1.831 (13%)	0.453 (49%)	0.126 (45%)	0.227 (187%)
	41	1.772 (16%)	0.421 (52%)	0.127 (45%)	0.239 (203%)
POD-Galerkin-E	25	1.239 (41%)	0.389 (56%)	0.072 (69%)	0.132 (67%)
	41	1.268 (40%)	0.210 (76%)	0.055 (76%)	0.085 (8%)
POD-Galerkin-R	25	2.055 (5%)	0.809 (8%)	0.231 (0.4%)	0.111 (41%)
	41	1.820 (14.5%)	0.744 (16%)	0.235 (2%)	0.144 (82%)

Table 5: Time-averaged amplitudes of POD modes from DNS and the reduced-order models. Here, the numbers in the parenthesis indicate the relative error to the values from DNS.

633 some physical processes which are not simply resolved by the increase in the number of plane
634 Fourier modes (i.e. M_x and M_z). In this respect, it is worth reminding that the reduced-order
635 models in the present study only consider the leading POD mode for each (n_x, n_z) . It is
636 therefore presumable that the compensation made by the eddy viscosity model is associated
637 with the lack of the higher-order POD modes for each (n_x, n_z) .

638 4.5. Comparison of the reduced-order models

639 Having examined all of the reduced-order models introduced in §3, their performance is
640 compared in this subsection. Table 5 shows the time-averaged amplitudes of the four leading
641 POD modes from DNS and the reduced-order models, except the POD-SINDy model whose
642 solution was found to blow up (see §4.2). We note that the four POD modes contain
643 approximately 95% of total perturbation kinetic energy (see table 1). The POD-Galerkin
644 model performs sensibly only for the mean component, $a_{0,0}^{(1)}$, while the rest of the components
645 with $(n_x, n_z) \neq (0, 0)$ exhibit considerable errors ranging from 50% to 200%. The addition
646 of an empirical eddy viscosity does not improve the POD-Galerkin model greatly (i.e. POD-
647 Galerkin-E model), since the model still shows errors of 50%-80% across all the four leading
648 POD modes. This model may also be viewed to perform most poorly, given the largest errors
649 for $a_{0,0}^{(1)}$ that contains the largest amount of perturbation energy. Finally, the POD-Galerkin-R
650 model shows the best performance and it has only a maximum 16% error for the first three
651 leading POD modes. Although this model still shows a relatively large error for $a_{1,1}^{(1)}$, the
652 energy contained by this mode in DNS is only about 1% (see table 1). Therefore, this error
653 would be relatively insignificant.

654 The mean and turbulent velocity fluctuations from DNS and the reduced-order models
655 are compared in figure 7. As expected from table 5, the mean velocity from the POD-
656 Galerkin model and the POD-Galerkin-R model shows the best agreement with that from
657 DNS. However, the POD-Galerkin model exhibits large differences in the velocity fluctuation
658 profiles, while the statistics from the POD-Galerkin-E model are overall damped. A closer
659 inspection reveals that the cross-stream and wall-normal turbulence fluctuations are predicted
660 better by the 41-mode model, with a slightly poorer prediction in the streamwise mean velocity
661 as compared to the 25 mode model. In any case, the level of agreement of the POD-Galerkin-
662 R models in turbulence statistics has not been observed in any of the previous reduced-order
663 models in plane Couette flow (e.g. Smith *et al.* 2005; Cavalieri 2021).

664 Next, to assess the dynamical behaviour of the leading POD modes from the reduced-order

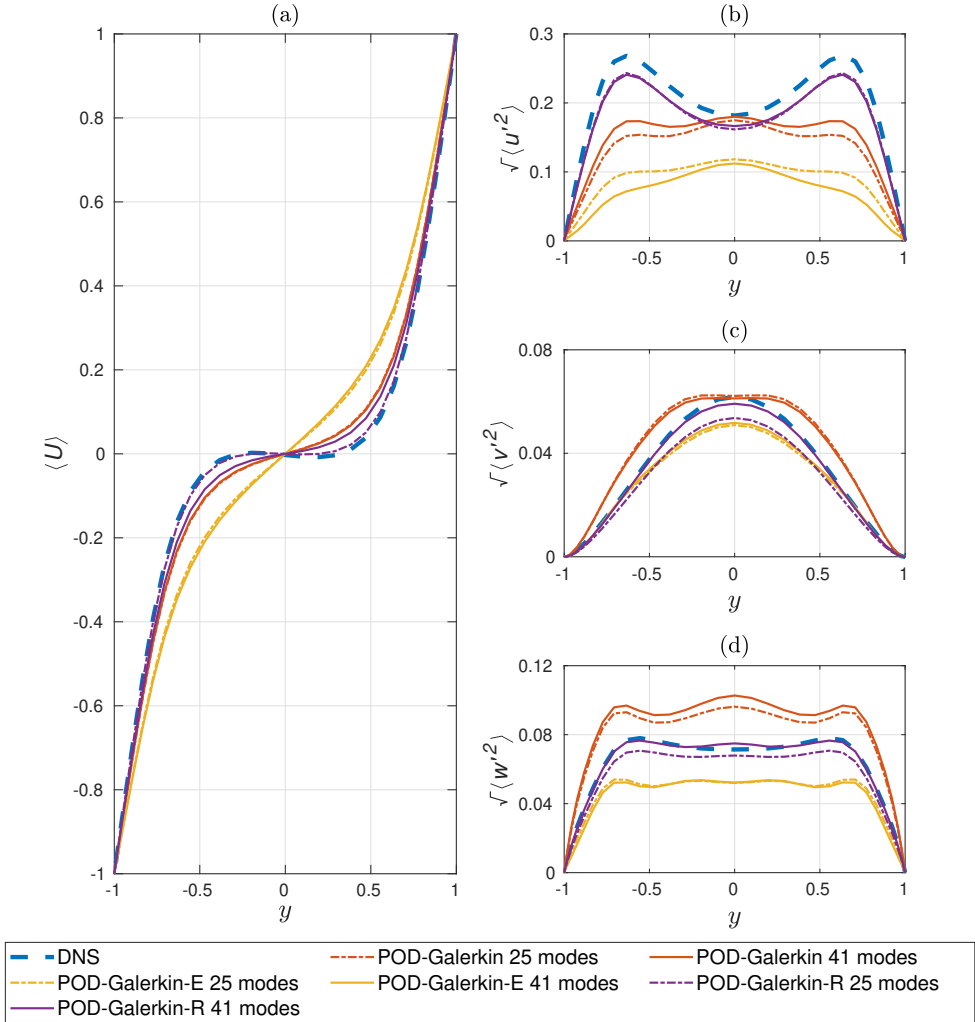


Figure 7: Turbulence statistics from DNS and the reduced-order models: (a) streamwise mean velocity; (b,c,d) root-mean-squared velocity fluctuations.

665 models, the following temporal auto- and cross-correlations of the main observables defined
 666 in (2.2) are computed:

$$667 \quad C_{(m_x, m_z)}^{(n_x, n_z)}(\tau) = \frac{\langle \tilde{M}(t + \tau; n_x, n_z) \tilde{M}(t; m_x, m_z) \rangle}{\sqrt{\tilde{M}^2(t; n_x, n_z)} \sqrt{\tilde{M}^2(t; m_x, m_z)}}, \quad (4.3)$$

668 where $\tilde{M}(t; n_x, n_z) = M(t; n_x, n_z) - \langle M(t; n_x, n_z) \rangle$. Figure 8 compares the correlation
 669 functions of the 25-mode and 41-mode models considered with those of DNS. In general,
 670 for the temporal correlations of $C_{(0,1)}^{(0,1)}$, the POD-Galerkin-R model have a closer match to
 671 the DNS data when compared to POD-Galerkin and POD-Galerkin-E models. The inclusion
 672 of more POD modes have the effect of improving the correlations of $C_{(1,1)}^{(1,1)}$ especially for
 673 $\tau = [-15, 15]$. By doing so, we observe a notable improvement of the $C_{(0,1)}^{(1,1)}$ correlations, an

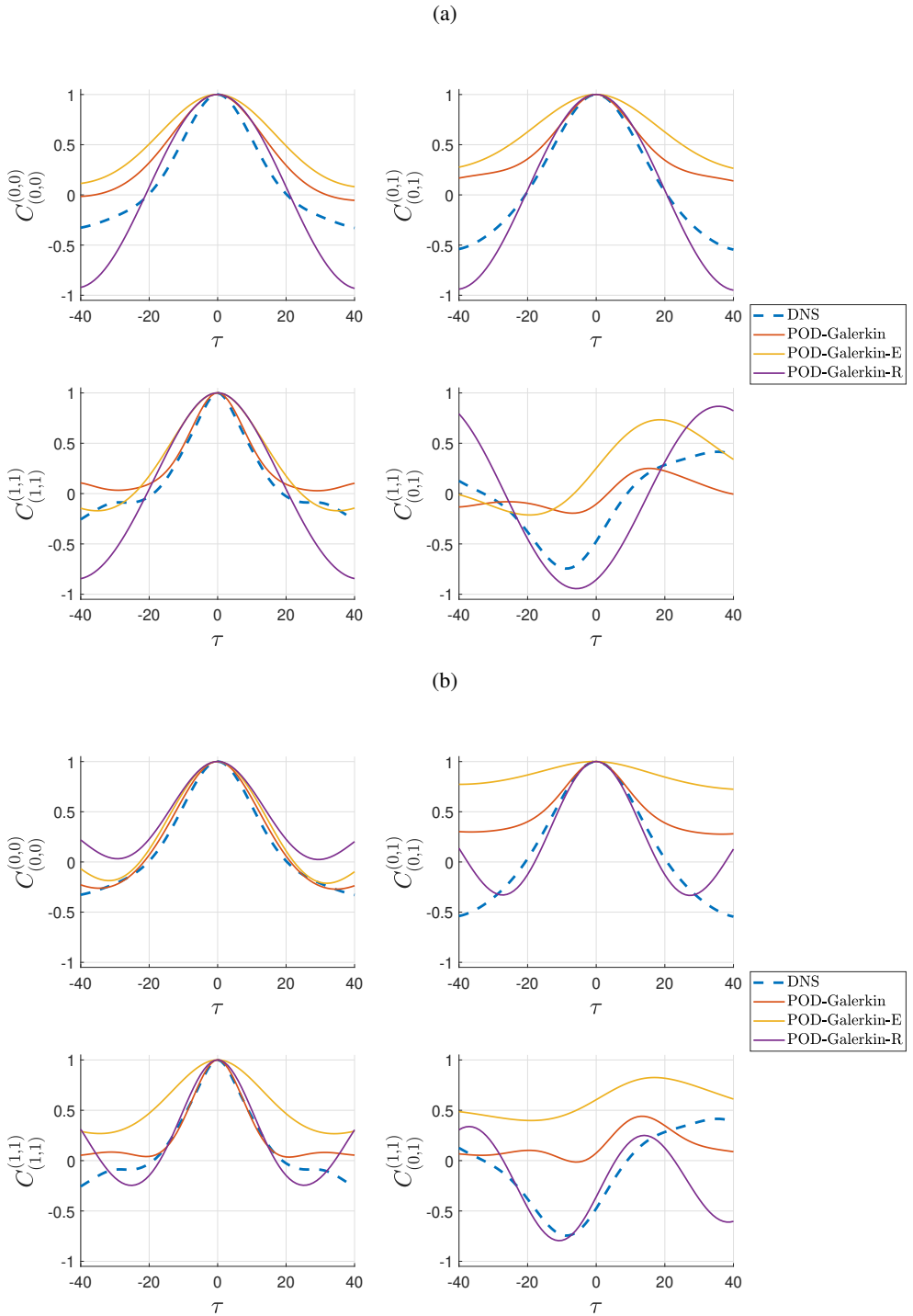


Figure 8: Temporal auto- and cross-correlations of: (a) 25-modes ($\gamma_e = 0.0005$ for the POD-Galerkin-R model); (b) 41-modes ($\gamma_e = 0.0001$ for the POD-Galerkin-R model).

674 important behaviour expected from the self-sustaining process, as it captures the breakdown
 675 of a streak structure and the regeneration of the streamwise vortices. Neither the POD-
 676 Galerkin or the POD-Galerkin-E model was able to closely replicate this behaviour with the
 677 inclusion of more POD modes.

678 Finally, figure 9 shows a time trace of the observables defined in (2.2) and a set of
 679 flow-field snapshots visualising a self-sustaining process generated by the POD-Galerkin-
 680 R 41-mode model. The strong streaky motions are apparent in $t = 1840 - 1857$, shown
 681 as a peak in $M(0, 1)$ in figure 9b. The streaks breakdown into a wavy-behaviour from
 682 $t = 1874 - 1891$, accompanied by a decrease in $M(0, 1)$ and an increase in $M(1, 0)$ in figure
 683 9b. The streaks breakdown completely from $t = 1909 - 1926$ while the quasi-streamwise
 684 vortices are regenerated, leading to an increase in $M(1, 1)$. Finally, the quasi-streamwise
 685 vortices feed energy to the streaks from $t = 1943 - 1960$, known as the 'lift-up' effect. We note
 686 that the self-sustaining process from the POD-Galerkin-R 41-mode model is qualitatively
 687 similar to that of figure 1, supporting the good agreements in temporal auto- and cross-
 688 correlations of figure 8.

689 5. Concluding remarks

690 In the present study, we have examined a set of physics-informed and data-driven approaches
 691 towards the development of a low-dimensional model more accurate than the conventional
 692 ones for turbulent wall-bounded shear flows. Based on the utilisation of POD modes, a
 693 particular focus is given to the case where the number of the POD modes is not necessarily
 694 large enough to cover the full dynamics of the given chaotic state. Starting from the
 695 conventional POD-Galerkin model, three additional approaches have been examined: 1)
 696 sparse regression of the POD-Galerkin dynamics (POD-SINDy model); 2) POD-Galerkin
 697 projection with an empirical eddy viscosity model (POD-Galerkin-E model; Smith *et al.*
 698 2005); 3) a newly-proposed POD-Galerkin projection with an optimal eddy viscosity
 699 determined using a sparse regression (POD-Galerkin-R model). The sparse regression of
 700 the POD-Galerkin dynamics has been found to be unsuccessful presumably due to the
 701 small number of POD modes considered, although this might be able to be improved
 702 by incorporating the energy-preserving nonlinearity constraint into the model (Loiseau &
 703 Brunton 2018). In the present study, this issue can be tackled by introducing a data-driven
 704 eddy-viscosity model for a highly turbulent flow, as the POD-Galerkin projection with a
 705 sparse optimal viscosity has been found to well approximate the given chaotic dynamics.
 706 It should be mentioned that this eddy-viscosity model was introduced to have a better
 707 nonlinear energy balance (3.8) only at large scale spanned by the POD modes of interest (see
 708 also discussion in §3.3). In this respect, the data-driven eddy viscosity model here may be
 709 viewed to be a pragmatic alternative of the the energy-preserving nonlinearity constraint in
 710 Loiseau & Brunton (2018) for highly turbulent flows.

711 The key reason to the success of the POD-Galerkin-R model is that it considers the largest
 712 amount of physical information: i.e. Galerkin projection and energy cascade. It is important
 713 to emphasise that the Galerkin projection allows the reduced-order model to inherit the
 714 mathematical structure of the Navier-Stokes equations. In other words, this feature makes
 715 the reduced-order model analysable, as it contains all the mathematical elements previously
 716 utilised to study the flow physics: e.g. linearised dynamics and production/dissipation, etc.
 717 Having said this, the energy cascade via nonlinear and non-local interactions modelled here
 718 is still an active and challenging research topic (e.g. Vassilicos 2015), and it may take years
 719 to gain the full physical understanding, if not possible. The eddy-viscosity model utilised in
 720 the present study is still very minimal to incorporate the full energy cascade dynamics into
 721 a reduced-order model. However, a notable point of doing so is that a data-driven approach

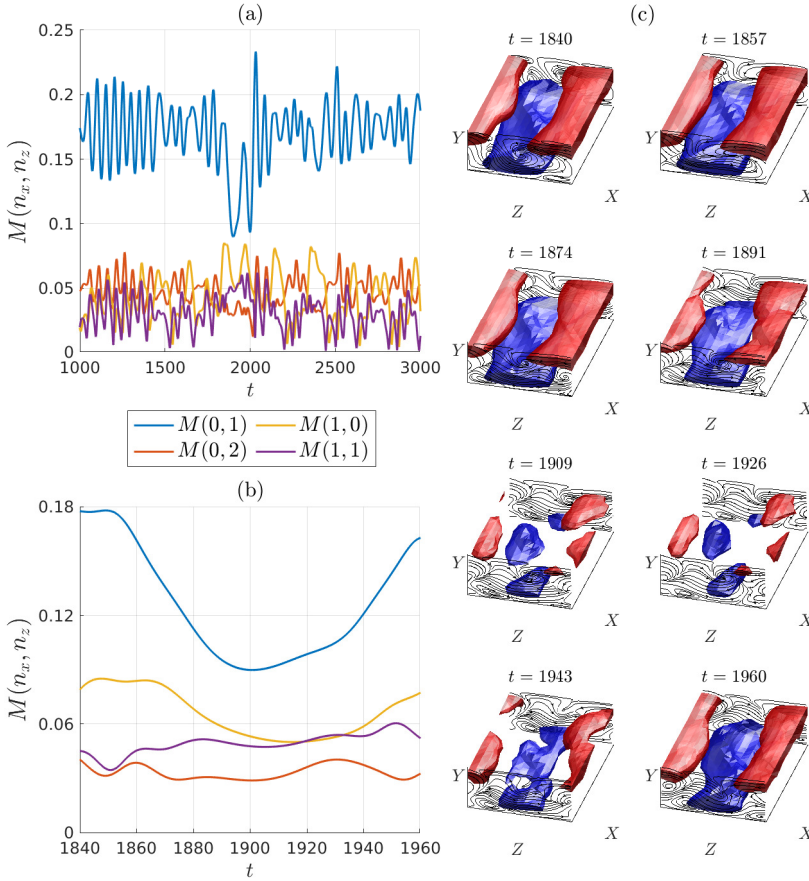


Figure 9: Time trace of $M(0, 1)$, $M(0, 2)$, $M(1, 0)$, $M(1, 1)$ obtained from the POD-Galerkin-R 41 mode model (a) for $t = 1000 - 3000$ and (b) for $t = 1840 - 1960$. (c) Flow snapshots at $t = 1840, 1857, 1874, 1891, 1909, 1926, 1943, 1960$, where the blue and red iso-surfaces indicate $u = \pm 0.38$, respectively.

722 (i.e. sparse regression), which itself does not provide any insight into the given flow physics,
 723 was applied to model the flow physics which is not fully understood. We have shown that
 724 classical physics-based reduced-order modelling (i.e. POD-Galerkin) of a complex process is
 725 limited, and data-driven approaches can be exploited to improve the reduced-order models.

726 It should also be mentioned that there have recently been a surge of data-driven flow
 727 modelling approaches using optimisation and machine learning (see the recent review by
 728 Brunton *et al.* 2020). In the context of reduced-order modelling, utilisation of some machine
 729 learning algorithms (e.g. reservoir computing) was proposed for the prediction of a chaotic
 730 dynamical system (e.g. Pathak *et al.* 2018 and the other recent studies). While such an
 731 approach may well be practically useful for the prediction of extreme events relevant to
 732 weather forecasting, it does not offer insights into the flow physics required for modelling
 733 in a wider context. Indeed, how one would smartly incorporate the known flow physics into
 734 a data-driven modelling approach has been a central issue of many current investigations,
 735 especially when the equations of motion (e.g. Navier-Stokes equations) are fully available. In

736 this respect, the utilisation of Galerkin projection in the present study may perhaps provide a
 737 new opportunity as it directly offers a mathematical structure from the governing equations.
 738 Indeed, instead of utilising a model given by (3.13), a highly flexible form of model for \mathbf{T}
 739 may well be considered with a machine learning algorithm.

740 It is also worth mentioning about the extrapolation capability of the model obtained at
 741 a given set of parameters to the others. This issue has often been regarded to be generally
 742 challenging for a model reduction problem. In the present study, the optimal eddy viscosity
 743 obtained here is, in fact, intricately linked to the physical processes of the given system. The
 744 optimal value would vary with the change of system parameters (e.g. the Reynolds-number
 745 dependent role of small scales modelled with the eddy viscosity here). Therefore, further
 746 efforts need to be made to address this issue in the future.

747 Finally, given the original scope of the present paper discussed in §1.1, the natural next
 748 step of the present study is to apply the approach proposed here to flows at higher Reynolds
 749 numbers where coherent structures begin to emerge at multiple integral length scales as
 750 in the attached eddy hypothesis of Townsend (1956, 1976). An obvious issue for this next
 751 step would lie in the determination of the number of POD modes that capture the core
 752 interaction dynamics at integral length scales, while effectively excluding the dissipative
 753 dynamics that can be modelled using the data-driven eddy-viscosity approach here. Once
 754 this process is completed with an appropriate validation using DNS data, invariant solutions
 755 (e.g. unstable periodic orbits) of the reduced-order model can subsequently be computed to
 756 study the multi-scale dynamics. The current hope is that the total degree of freedom of the
 757 reduced-order model remains at $O(10^2 - 10^3)$ at a sufficiently high Reynolds number (e.g.
 758 $Re_\tau \approx 500 - 1000$) to tackle this challenge.

759 Funding

760 Y.H. gratefully acknowledges the financial support of the Leverhulme Trust (RPG-2019-123)
 761 and the Engineering and Physical Sciences Research Council (EPSRC; EP/T009365/1) in
 762 the UK.

763 Declaration of interest

764 The authors report no conflict of interest.

765 Appendix A. Galerkin projection

766 The projection of (2.4a) onto the Navier-Stokes equations (2.1) leads to the following system
 767 of ordinary differential equations:

$$768 \quad \dot{a}_{n_x, n_z}^{(n)} = \sum_{m=1}^{N_p} L_{n_x, n_z}^{(n, m)} a_{n_x, n_z}^{(m)} + \mathcal{N}_{n_x, n_z}^{(n)}, \quad (\text{A } 1a)$$

769 where

$$770 \quad \mathcal{N}_{n_x, n_z}^{(n)} = \sum_{k_x=-N_x}^{N_x} \sum_{k_z=-N_z}^{N_z} \sum_{k=1}^{N_p} \sum_{m=1}^{N_p} N_{n_x, n_z}^{(n, k, m)} a_{k_x, k_z}^{(k)} a_{m_x=n_x-k_x, m_z=n_z-k_z}^{(m)}, \quad (\text{A } 1b)$$

772 with

$$L_{n_x, n_z}^{(n,m)} = -\frac{1}{Re} \left[\left(\frac{2\pi n_x}{L_x} \right)^2 + \left(\frac{2\pi n_z}{L_z} \right)^2 \right] \delta_{nm} - \frac{1}{Re} \int_y \left(\frac{d\phi_{n_x, n_z}^{(m)}}{dy} \right)^H \frac{d\phi_{n_x, n_z}^{(n)}}{dy} dy$$

$$- \left(\frac{2\pi i n_x}{L_x} \right) \int_y y (\phi_{n_x, n_z}^{(m)})^H \phi_{n_x, n_z}^{(n)} dy - \int_y (\phi_{2, n_x, n_z}^{(m)})^H \phi_{1, n_x, n_z}^{(n)} dy,$$
(A 1c)

775 and

$$N_{n_x, n_z}^{(n,k,m)} = -\frac{1}{\sqrt{L_x L_z}} \int_y (\phi_{n_x, n_z}^{(n)})^H \left[\frac{2\pi i k_x}{L_x} \phi_{k_x, k_z}^{(k)} \frac{d\phi_{k_x, k_z}^{(k)}}{dy} - \frac{2\pi i k_z}{L_z} \phi_{k_x, k_z}^{(k)} \right] \phi_{m_x = n_x - k_x, m_z = n_z - k_z}^{(m)} dy,$$
(A 1d)

776 Therefore, (A 1) may be written as the following quadratic nonlinear dynamical system form:
777

$$\dot{\mathbf{a}} = \mathbf{L}\mathbf{a} + \mathbf{N}(\mathbf{a}, \mathbf{a}),$$
(A 2a)

780 where \mathbf{a} is defined as a column vector, each element of which is given by $a_{n_x, n_z}^{(n)}$,

$$\mathbf{L}\mathbf{a} \equiv \sum_{m=1}^{N_p} L_{n_x, n_z}^{(n,m)} a_{n_x, n_z}^{(m)},$$
(A 2b)

782 and

$$\mathbf{N}(\mathbf{a}, \mathbf{a}) \equiv \mathcal{N}_{n_x, n_z}^{(n)}.$$
(A 2c)

784 Similarly, the diffusion operator used for the eddy-viscosity closure in §3.3 and §3.4 is
785 defined as

$$\mathbf{D}\mathbf{a} \equiv \sum_{m=1}^{N_p} D_{n_x, n_z}^{(n,m)} a_{n_x, n_z}^{(m)},$$
(A 3a)

787 where

$$D_{n_x, n_z}^{(n,m)} = -\left[\left(\frac{2\pi n_x}{L_x} \right)^2 + \left(\frac{2\pi n_z}{L_z} \right)^2 \right] \delta_{nm} - \int_y \left(\frac{d\phi_{n_x, n_z}^{(n)}}{dy} \right)^H \frac{d\phi_{n_x, n_z}^{(m)}}{dy} dy$$
(A 3b)

789 for $(n_x, n_z) \neq (0, 0)$ and

$$D_{n_x, n_z}^{(n,m)} = 0.$$
(A 3c)

791 for $(n_x, n_z) = (0, 0)$, so that the eddy viscosity is not applied to the mean equation. Using
792 the diffusion operator above, the eddy viscosity model defined in (3.13) is finally written as

$$\mathbf{V}_t \mathbf{D}\mathbf{a} \equiv c_{n_x, n_z}^{(n)} e(t) \sum_{m=1}^{N_p} D_{n_x, n_z}^{(n,m)} a_{n_x, n_z}^{(m)},$$
(A 4a)

794 where $c_{n_x, n_z}^{(n)}$ forms each element of \mathbf{c} in (3.13).

795 Appendix B. The choice of e in §3.4

796 Here, we report a POD-Galerkin-R model, in which $e(t) = \mathbf{a}^H \mathbf{a}$ is considered instead
797 of $e(t) = a_{0,0}^{(1)}$. The sparse regression in (3.16) is performed with the DNS data for $t \in$
798 $[-10000, 0]$ and the resulting model is subsequently examined for $t \in [0, 5000]$. The time
799 trace of $M(n_x, n_z)$ from the reduced-order model and from DNS is shown in figure 10.

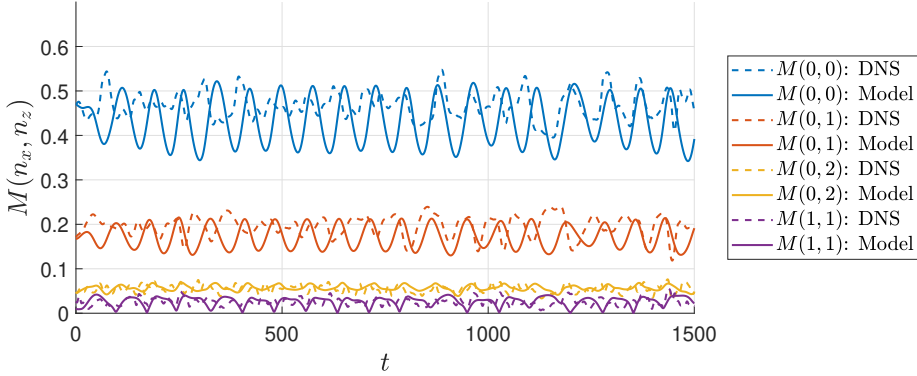


Figure 10: Time trace of $M(n_x, n_z)$ from DNS and the POD-Galerkin-R model ($\gamma_e = 0.0005$ and $e(t) = \mathbf{a}^H \mathbf{a}$) with 25 modes.

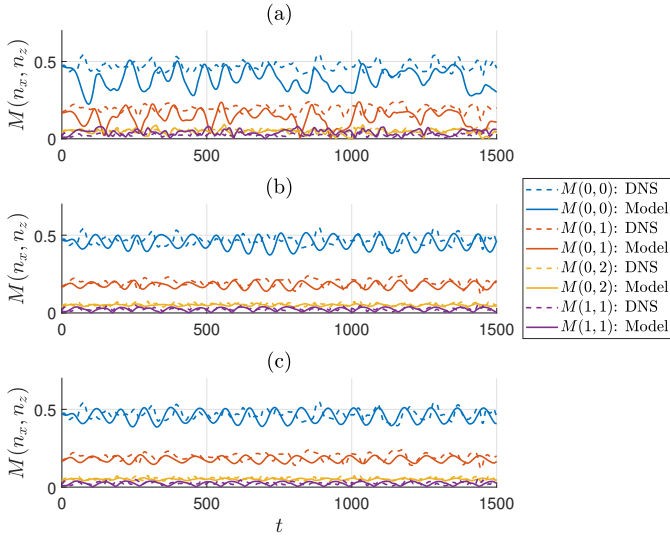


Figure 11: Time trace of $M(n_x, n_z)$ from DNS and the POD-Galerkin-R of the 25-mode model : (a) $\gamma_e = 0.001$; (b) $\gamma_e = 0.0005$; (c) $\gamma_e = 0.0003$.

800 Overall, the mean of $M(n_x, n_z)$ and its oscillation time scale from the reduced-order model
 801 compare fairly well with those from DNS. The oscillation magnitude of $M(0, 0)$ in this case
 802 is slightly stronger than that from the POD-Galerkin-R model with $e(t) = a_{0,0}^{(1)}$ (figure 5a),
 803 and the oscillation appears to be slightly less chaotic.

804 Appendix C. The effect of γ_e on model dynamics.

805 The sparsity-promoting ℓ_1 -regulariser acts as a control parameter balancing between the
 806 effect of the GP model and the residual model on the overall dynamics. In Figure 11, we
 807 observe that for $\gamma_e = 0.001$, the effect of the residual model adversely affects the temporal
 808 dynamics as only certain POD modes are being selectively damped. For $\gamma_e = 0.0003$, the

809 residual model dominates and the POD modes are strongly coupled to the mean POD mode
 810 where we obtain oscillatory behaviour due to excessive damping.

REFERENCES

- 811 DEL ÁLAMO, J.C. & JIMÉNEZ, J. 2003 Spectra of the very large anisotropic scales in turbulent channels. *Phys.*
 812 *Fluids* **15**, L41.
- 813 DEL ÁLAMO, J. C. & JIMÉNEZ, J. 2006 Linear energy amplification in turbulent channels. *J. Fluid Mech.* **559**,
 814 205–213.
- 815 ALIZARD, F. 2015 Linear stability of optimal streaks in the log-layer of turbulent channel flows. *Phys. Fluids*
 816 **27**, 105103.
- 817 AUBRY, N., HOLMES, P., LUMLEY, J. L. & STONE, E. 1988 The dynamics of coherent structures in the wall
 818 region of a turbulent boundary layer. *J. Fluid Mech.* **192**, 115–173.
- 819 AVILA, K., MOXEY, D., DE LOZAR, A., AVILA, M., BARKLEY, D. & HOF, BJORN 2011 The onset of turbulence
 820 in pipe flow. *Science* **333**, 192–196.
- 821 BARKLEY, D. 2016 Theoretical perspective on the route to turbulence in a pipe. *Journal of Fluid Mechanics*
 822 **803**.
- 823 BEETHAM, S. & CAPECELATRO, J. 2020 Formulating turbulence closures using sparse regression with
 824 embedded form invariance. *Physical Review Fluids* **5** (8).
- 825 BEETHAM, S., FOX, R.O. & CAPECELATRO, J. 2021 Sparse identification of multiphase turbulence closures
 826 for coupled fluid–particle flows. *Journal of Fluid Mechanics* **914**, A11.
- 827 BEWLEY, T. R., MOIN, P. & TEMAM, R. 2001 Dns-based predictive control of turbulence: an optimal
 828 benchmark for feedback algorithms. *J. Fluid Mech.* **447**, 179–225.
- 829 BRUNTON, STEVEN L & KUTZ, J NATHAN 2019 *Data-driven science and engineering: Machine learning,*
 830 *dynamical systems, and control*. Cambridge University Press.
- 831 BRUNTON, S. L., NOACK, B. R. & KOUMOUTSAKOS, P. 2020 Machine learning for fluid mechanics. *Annu.*
 832 *Rev. of Fluid Mec.* **52**, 477–508.
- 833 BRUNTON, STEVEN L., PROCTOR, JOSHUA L. & KUTZ, J. NATHAN 2016 Discovering governing equations from
 834 data by sparse identification of nonlinear dynamical systems. *Proceedings of the National Academy*
 835 *of Sciences* **113** (15), 3932–3937, arXiv: <https://www.pnas.org/content/113/15/3932.full.pdf>.
- 836 BUTLER, K. M. & FARRELL, B. F. 1993 Optimal perturbations and streak spacing in wall-bounded turbulent
 837 shear flow. *Phys. Fluids* **5**, 774–777.
- 838 CALLAHAM, J. L., BRUNTON, S. L. & LOISEAU, J.-C. 2021a On the role of nonlinear correlations in reduced-
 839 order modeling. *arXiv preprint arXiv:2106.02409* ArXiv:2106.02409.
- 840 CALLAHAM, J. L., LOISEAU, J.-C., RIGAS, G. & BRUNTON, S. L. 2021b Nonlinear stochastic modelling with
 841 langevin regression. *Pro. Roy. Soc. Lond. A* **477** (2250), 487–505.
- 842 CASSINELLI, A., DE GIOVANNI, M. & HWANG, Y. 2017 Streak instability in near-wall turbulence revisited.
 843 *J. Turbul.* **18** (5), 443–464.
- 844 CAVALIERI, A. V. G. 2021 Structure interactions in a reduced-order model for wall-bounded turbulence.
 845 *Phys. Rev. Fluids* **6**, 034610.
- 846 CHANTRY, M., TUCKERMAN, L. S. & BARKLEY, D. 2017 Universal continuous transition to turbulence in a
 847 planar shear flow. *J. Fluid Mech.* **824**, R1.
- 848 CHO, M., HWANG, Y. & CHOI, H. 2018 Scale interactions and spectral energy transfer in turbulent channel
 849 flow. *J. Fluid Mech.* **854**, 474–504.
- 850 CHOI, H., TEMAM, R., MOIN, P. & KIM, J 1993 Feedback control for unsteady flow and its application to the
 851 stochastic burgers equation. *J. Fluid Mech.* **245**, 509–543.
- 852 CORDIER, LAURENT, EL MAJD, B ABOU & FAVIER, JULIEN 2010 Calibration of pod reduced-order models
 853 using tikhonov regularization. *International journal for numerical methods in fluids* **63** (2), 269–296.
- 854 COSSU, C., PUJALS, G. & DEPARDON, S. 2009 Optimal transient growth and very large scale structures in
 855 turbulent boundary layers. *J. Fluid Mech.* **619**, 79–94.
- 856 COUPLET, M, BASDEVANT, C & SAGAUT, P 2005 Calibrated reduced-order pod-galerkin system for fluid flow
 857 modelling. *Journal of Computational Physics* **207** (1), 192–220.
- 858 COUPLET, M, SAGAUT, P & BASDEVANT, C 2003 Intermodal energy transfers in a proper orthogonal
 859 decomposition–galerkin representation of a turbulent separated flow. *Journal of fluid mechanics*
 860 **491** (491), 275–284.

- 861 CRISANTI, A., JENSEN, M. H., PALADIN, G. & VULPIANI, A. 1993 Predictability of velocity and temperature
862 fields in intermittent turbulence. *J. Phys. A* **26**, 6943.
- 863 DOOHAN, P., BENGANA, Y., YANG, Q., WILLIS, A. P. & HWANG, Y. 2021a Multi-scale state space and travelling
864 waves in wall-bounded turbulence. *J. Fluid Mech.* Under review.
- 865 DOOHAN, P., WILLIS, A. P. & HWANG, Y. 2019 Shear stress-driven flow: the state space of near-wall turbulence
866 as $Re_\tau \rightarrow \infty$. *J. Fluid Mech.* **874**, 606–638.
- 867 DOOHAN, P., WILLIS, A. P. & HWANG, Y. 2021b Minimal multi-scale dynamics of near-wall turbulence. *J.*
868 *Fluid Mech.* **913**, A8.
- 869 DURAISAMY, KARTHIK 2021 Perspectives on machine learning-augmented reynolds-averaged and large eddy
870 simulation models of turbulence. *Phys. Rev. Fluids* **6**, 050504.
- 871 ECKHARDT, B., SCHNEIDER, T.M., HOF, B. & WESTERWEEL, J. 2007 Turbulence Transition in Pipe Flow. *Ann.*
872 *Rev. Fluid Mech.* **39**, 447.
- 873 FAISST, H. & ECKHARDT, B. 2003 Travelling waves in pipe flow. *Phys. Rev. Lett.* **91**, 224502.
- 874 FALCO, R. E. 1977 Coherent motions in the outer region of turbulent boundary layers. *Phys. Fluids* **20**,
875 S124–S132.
- 876 FARAZMAND, M. 2016 An adjoint-based approach for finding invariant solutions of navier–stokes equations.
877 *J. Fluid Mech.* **795**, 278–312.
- 878 FLORES, O. & JIMÉNEZ, J. 2010 Hierarchy of minimal flow units in the logarithmic layer. *Phys. Fluids* **22**,
879 071704.
- 880 GELSS, PATRICK, KLUS, STEFAN, EISERT, JENS & SCHÜTTE, CHRISTOF 2019 Multidimensional approximation
881 of nonlinear dynamical systems. *Journal of Computational and Nonlinear Dynamics* **14** (6).
- 882 GIBSON, J. F., HALCROW, J. & CVITANOVIC, P. 2008 Visualizing the geometry of state space in plane Couette
883 flow. *J. Fluid Mech.* **611**, 107–130.
- 884 GIBSON, J. F., HALCROW, J. & CVITANOVIC, P. 2009 Equilibrium and traveling-wave solutions of plane
885 Couette flow. *J. Fluid Mech.* **638**, 243–266.
- 886 DE GIOVANNETTI, M., SUNG, H. J. & HWANG, Y. 2017 Streak instability in turbulent channel flow: the seeding
887 mechanism of large-scale motions. *J. Fluid Mech.* **832**, 483–513.
- 888 GRAHAM, M. D. & FLORYAN, D. 2020 Exact coherent states and the nonlinear dynamics of wall-bounded
889 turbulent flows. *Annu. Rev. Fluid. Mech.* **53**, 227–253.
- 890 HALL, P. & SHERWIN, S. J. 2010 Streamwise vortices in shear flows: harbingers of transition and the skeleton
891 of coherent structures. *J. Fluid Mech.* **661**, 178–205.
- 892 HAMILTON, JAMES M., KIM, JOHN & WALEFFE, FABIAN 1995 Regeneration mechanisms of near-wall
893 turbulence structures. *Journal of Fluid Mechanics* **287** (1), 317–348.
- 894 HEAD, M. R. & BANDYOPADHAY, P. 1981 New aspects of turbulent boundary-layer structure. *J. Fluid Mech*
895 **107**, 297–338.
- 896 HOLMES, PHILIP, LUMLEY, JOHN L. & BERKOOZ, GAL 1996 *Turbulence, Coherent Structures, Dynamical*
897 *Systems and Symmetry. Cambridge Monographs on Mechanics*. Cambridge University Press.
- 898 HUTCHINS, N. & MARUSIC, I. 2007 Evidence of very long meandering features in the logarithmic region of
899 turbulent boundary layers. *J. Fluid Mech.* **579**, 1–28.
- 900 HWANG, Y. 2015 Statistical structure of self-sustaining attached eddies in turbulent channel flow. *J. Fluid*
901 *Mech.* **723**, 264–288.
- 902 HWANG, Y. & BENGANA, Y. 2016 Self-sustaining process of minimal attached eddies in turbulent channel
903 flow. *J. Fluid Mech.* **795**, 708–738.
- 904 HWANG, Y. & COSSU, C. 2010a Amplification of coherent streaks in the turbulent Couette flow: an input-
905 output analysis at low Reynolds number. *J. Fluid Mech.* **643**, 333–348.
- 906 HWANG, Y. & COSSU, C. 2010b Linear non-normal energy amplification of harmonic and stochastic forcing
907 in the turbulent channel flow. *J. Fluid Mech.* **664**, 51–73.
- 908 HWANG, Y. & COSSU, C. 2010c Self-sustained process at large scales in turbulent channel flow. *Phys. Rev.*
909 *Lett.* **105**, 044505.
- 910 HWANG, Y. & COSSU, C. 2011 Self-sustained processes in the logarithmic layer of turbulent channel flows.
911 *Phys. Fluid* **23**, 061702.
- 912 HWANG, Y. & LEE, M. 2020 The mean logarithm emerges with self-similar energy balance. *J. Fluid Mech.*
913 **903**, R6.
- 914 HWANG, Y., WILLIS, A. P. & COSSU, C. 2016 Invariant solutions of minimal large-scale structures in turbulent
915 channel flow for Re_τ up to 1000. *J. Fluid Mech.* **802**, R1.
- 916 JEONG, J., BENNEY, F., SCHOPPA, W. & KIM, J. 1997 Coherent structures near the wall in a turbulent channel
917 flow. *J. Fluid Mech.* **332**, 185–214.

- 918 JIMÉNEZ, JAVIER & MOIN, PARVIZ 1991 The minimal flow unit in near-wall turbulence. *Journal of Fluid*
919 *Mechanics* **225**, 213–240.
- 920 JIMÉNEZ, J. & SIMENS, M. P. 2001 Low-dimensional dynamics of a turbulent wall flow. *J. Fluid Mech.* **435**,
921 81–91.
- 922 JOSEPH, D. D. 1976 *Stability of Fluid Motions. Springer Tracts in Natural Philosophy, vol. 27*. New York:
923 Springer.
- 924 KAWAHARA, G. & KIDA, S. 2001 Periodic motion embedded in plane Couette turbulence: regeneration cycle
925 and burst. *J. Fluid Mech.* **449**, 291–300.
- 926 KAWAHARA, G., UHLMANN, M. & VAN VEEN, L. 2012 The significance of simple invariant solutions in
927 turbulent flows. *Annu. Rev. Fluid Mech.* **44**, 203–225.
- 928 KIM, K. C. & ADRIAN, R. 1999 Very large-scale motion in the outer layer. *Phys. Fluids* **11** (2), 417–422.
- 929 KLINE, S. J., REYNOLDS, W. C., SCHRAUB, F. A. & RUNSTADLER, P. W. 1967 The structure of turbulent
930 boundary layers. *J. Fluid Mech.* **30**, 741–773.
- 931 KOVASZNAY, L. S. G., KIBENS, V. & BLACKWELDER, R. F. 1970 Large-scale motion in the intermittent region
932 of a turbulent boundary layer. *J. Fluid Mech.* **41**, 283–325.
- 933 KREILOS, T. & ECKHARDT, B. 2012 Periodic orbits near onset of chaos in plane Couette flow. *Chaos* **22**,
934 047505.
- 935 LAGHA, M. & MANNEVILLE, P. 2007 Modelling transitional plane Couette flow. *Eur. Phys. J.* **58**, 433–447.
- 936 LEE, C., KIM, J. & CHOI, H. 1999 Suboptimal control of turbulent channel flow for drag reduction. *J. Fluid*
937 *Mech.* **358**, 245–258.
- 938 LEE, M. K. & MOSER, R. D. 2019 Spectral analysis of the budget equation in turbulent channel flows at high
939 reynolds number. *J. Fluid Mech.* **860**, 886–938.
- 940 LOISEAU, JEAN-CHRISTOPHE & BRUNTON, STEVEN L 2018 Constrained sparse galerkin regression. *Journal*
941 *of Fluid Mechanics* **838**, 42–67.
- 942 LOZANO-DURÁN, A., NIKOLAIDIS, M.-A., CONSTANTINOU, N. C. & KARP, M. 2021 Cause-and-effect of linear
943 mechanisms sustaining wall turbulence. *J. Fluid Mech.* **914**, A8.
- 944 LUMLEY, J. L. 1967 The structure of inhomogeneous turbulent flows. In *Atmospheric Turbulence and Radio*
945 *Wave Propagation* (ed. A. M. Yaglom & V. I. Tatarski), *Nonlinear Problems of Fluid Dynamics*.
946 Nakua, Moscow.
- 947 LUMLEY, JOHN L 1981 Coherent structures in turbulence. In *Transition and turbulence*, pp. 215–242. Elsevier.
- 948 MARUSIC, I. & MONTY, J. P. 2019 Attached eddy model of wall turbulence. *Annu. Rev. Fluid Mech.* **51**,
949 49–74.
- 950 MOEHLIS, J., FAISST, H. & ECKHARDT, B. 2004 A low-dimensional model for turbulent shear flows. *New*
951 *Journal of Physics* **6**, 56.
- 952 MOEHLIS, J., FAISST, H. & ECKHARDT, B. 2005 Periodic orbits and chaotic sets in a low-dimensional model
953 for shear flows. *SIAM J. Appl. Dyn. Syst.* **4**, 352–376.
- 954 MOHEBUJAMAN, MUHAMMAD, REBHOLZ, LEO G & ILIESCU, TRAIAN 2019 Physically constrained data-driven
955 correction for reduced-order modeling of fluid flows. *International Journal for Numerical Methods*
956 *in Fluids* **89** (3), 103–122.
- 957 NAGATA, M. 1990 Three-dimensional finite-amplitude solutions in plane Couette flow: bifurcation from
958 infinity. *J. Fluid Mech.* **217**, 519–527.
- 959 NOACK, B. R., MORZÝNSKI, M. & TADMOR, G. 2011 *Reduced-Order Modelling for Flow Control (CISM*
960 *Courses and Lectures)*. Springer.
- 961 ÖSTH, J., NOACK, B. R., KRAJNOVIĆ, S., BARROS, D. & BORÉE, J. 2014 On the need for a nonlinear subscale
962 turbulence term in pod models as exemplified for a high-reynolds-number flow over an ahmed body.
963 *J. Fluid Mech.* **747**, 518–544.
- 964 PARK, J., HWANG, Y. & COSSU, C. 2011 On the stability of large-scale streaks in the turbulent Couette and
965 Poiseuille flows. *C. R. Mécanique* **339** (1), 1–5.
- 966 PARK, J. S. & GRAHAM, M. D. 2015 Exact coherent states and connections to turbulent dynamics in minimal
967 channel flow. *J. Fluid Mech.* **782**, 430–454.
- 968 PATHAK, J., HUNT, B., GIRVAN, M., LU, Z. & OTT, E. 2018 Model-free prediction of large spatiotemporally
969 chaotic systems from data: a reservoir computing approach. *Phys. Rev. Lett.* **120**, 024102.
- 970 PODVIN, BÉRENGÈRE 2009 A proper-orthogonal-decomposition-based model for the wall layer of a turbulent
971 channel flow. *Physics of Fluids* **21** (1), 015111, arXiv: <https://doi.org/10.1063/1.3068759>.
- 972 PROTAS, B., NOACK, B. R. & ÖSTH, J. 2015 Optimal nonlinear eddy viscosity in galerkin models of turbulent
973 flows. *J. Fluid Mech.* **766**, 337–367.

- 974 RAWAT, S., COSSU, C., HWANG, Y. & RINCON, F. 2015 On the self-sustained nature of large-scale motions in
975 turbulent Couette flow. *J. Fluid Mech.* **782**, 515–540.
- 976 REMPFER, D. & FASEL, F. H. 1994a Dynamics of three-dimensional coherent structures in a flat-plate
977 boundary-layer. *J. Fluid Mech.* **275**, 257–283.
- 978 REMPFER, D. & FASEL, F. H. 1994b Evolution of three-dimensional coherent structures in a flat-plate
979 boundary-layer. *J. Fluid Mech.* **260**, 351–375.
- 980 RUBINI, R., LASAGNA, D. & RONCH, A. DA 2021 The I_1 -based sparsification of energy interactions in
981 unsteady lid-driven cavity flow. *J. Fluid Mech.* **905**, A18.
- 982 RUELLE, D. 1979 Microscopic fluctuations and turbulence. *Phys. Lett. A* **72**, 81.
- 983 SCHMELZER, MARTIN, DWIGHT, RICHARD P & CINNELLA, PAOLA 2020 Discovery of algebraic reynolds-stress
984 models using sparse symbolic regression. *Flow, Turbulence and Combustion* **104** (2), 579–603.
- 985 SCHMIDT, M. & LIPSON, H. 2009 Distilling free-form natural laws from experimental data. *Science* **264**,
986 255–275.
- 987 SCHOPPA, W. & HUSSAIN, F. 2002 Coherent structure generation in near-wall turbulence. *J. Fluid Mech.* **453**,
988 57–108.
- 989 SIROVICH, L. 1987 Turbulence and the dynamics of coherent structures; part I: Coherent structures. *Q. Appl.*
990 *Math* **XLV** (3), 561–571.
- 991 SMITH, TR, MOEHLIS, J & HOLMES, PH 2005 Low-dimensional models for turbulent plane couette flow in a
992 minimal flow unit. *Journal of Fluid Mechanics* **538**, 71.
- 993 TOWNSEND, A. A. 1956 *The structure of turbulent shear flow*, 1st edn. Cambridge U. Press.
- 994 TOWNSEND, A. A. 1976 *The structure of turbulent shear flow*, 2nd edn. Cambridge U. Press.
- 995 VASSILICOS, J. C. 2015 Dissipation in turbulent flows. *Annu. Rev. Fluid Mech.* **47**, 95–114.
- 996 VISWANATH, D. 2007 Recurrent motions within plane Couette turbulence. *J. Fluid Mech.* **580**, 339–358.
- 997 WALEFFE, F. 1995 Hydrodynamic stability and turbulence: Beyond transients to a self-sustaining process.
998 *Stud. Appl. Math.* **95**, 319–343.
- 999 WALEFFE, F. 1997 On a self-sustaining process in shear flows. *Phys. Fluids* **9**, 883–900.
- 1000 WALEFFE, F. 2001 Exact coherent structures in channel flow. *J. Fluid Mech.* **435**, 93–102.
- 1001 WALEFFE, F. 2003 Homotopy of exact coherent structures in plane shear flows. *Phys. Fluids* **15**, 1517–1534.
- 1002 WEDIN, H. & KERSWELL, R. R. 2004 Exact coherent structures in pipe flow: travelling wave solutions. *J.*
1003 *Fluid Mech.* **508**, 333–371.
- 1004 WILLIS, A. P., CVITANOVIC, P. & AVILA, M. 2013 Revealing the state space of turbulent pipe flow by
1005 symmetry reduction. *J. Fluid Mech.* **721**, 514–540.
- 1006 YANG, Q., WILLIS, A. P. & HWANG, Y. 2019 Exact coherent states of attached eddies in channel flow. *J.*
1007 *Fluid Mech.* **862**, 1029–1059.